

## Cluster Weak Gravitational Lensing

KEIICHI UMETSU<sup>(1)(2)</sup>

<sup>(1)</sup> *Academia Sinica Institute of Astronomy and Astrophysics, P.O. Box 23-141, Taipei 10617, Taiwan*

<sup>(2)</sup> *Leung center for Cosmology and Particle Astrophysics, National Taiwan University, Taipei 10617, Taiwan*

**Summary.** — Weak gravitational lensing of background galaxies is a unique, direct probe of the distribution of matter in clusters of galaxies. We review several important aspects of cluster weak gravitational lensing together with recent advances in weak lensing techniques for measuring cluster lensing profiles and constraining cluster structure parameters.

2	1.	Introduction
2	2.	Basic Equations of Cosmological Gravitational Lensing
2	2'1.	Gravitational Deflection and Lens Equation
5	2'2.	Cosmological Lens Equation
7	2'3.	Cluster Gravitational Lensing
8	2'4.	Lensing Jacobian Matrix
10	2'5.	Lensing Convergence
10	2'6.	Quadrupole Shape Distortion: Gravitational Shear
11	2'7.	Area Distortion: Gravitational Magnification
12	3.	Weak Gravitational Lensing
12	3'1.	Weak Lensing Mass Reconstruction
15	3'2.	Weak Lensing Distortion Observables
18	3'3.	$E/B$ Decomposition
19	3'4.	Magnification Bias
20	4.	Cluster Weak Lensing Profiles
20	4'1.	Weak Lensing Distortion
21	4'2.	Weak Lensing Depletion
22	4'3.	Weak Lensing Dilution
24	4'4.	Aperture Mass Densitometry
26	4'5.	Weak Lensing Convergence
27	Appendix 1.	Multiple Lens Equation
28		References

## 1. – Introduction

Propagation of light rays from a distant source to the observer is governed by the gravitational field of intervening mass fluctuations as well as by the global geometry of the universe. The images of background sources hence carry the imprint of the gravitational potential of intervening cosmic structures, and their statistical properties can be used to test the background cosmological models.

The deep gravitational potential wells of clusters of galaxies generate weak shape distortions of the images of background sources due to differential deflection of light rays, resulting in a systematic distortion pattern of background source images around the center of massive clusters, known as weak gravitational lensing[1, 2, 3, 4, 5]. In the past decade, weak lensing has become a powerful, reliable measure to map the distribution of matter in clusters, dominated by invisible dark matter (DM), without requiring any assumption about the physical and dynamical state of the system[6, 7]. Recently, cluster weak lensing has been used to examine the form of DM density profiles[8, 9, 10, 11, 12, 13, 14, 15], aiming for an observational test of the equilibrium density profile of DM halos and the scaling relation between halo mass and concentration, predicted by  $N$ -body simulations in the standard Lambda Cold Dark Matter ( $\Lambda$ CDM) model[16, 17]. Weak lensing techniques have also been used to search for cluster-sized mass concentrations projected on the sky[18, 19, 20], allowing us to define samples of “shear-selected” DM halos from deep optical surveys[21, 22, 23].

In this lecture we briefly review several important aspects of cluster weak gravitational lensing. There have been several reviews of relevant subjects: For general treatments of gravitational lensing, we refer the reader to Schneider, Ehlers, & Falco[24], Blandford & Narayan[25], Refsdal & Surdej[26], and Narayan & Bartelmann[27]. For a review on strong gravitational lensing in clusters, see Hattori, Kneib, & Makino[28]. For a general review of weak gravitational lensing, see Bartelmann & Schneider[4].

## 2. – Basic Equations of Cosmological Gravitational Lensing

The local universe appears to be highly inhomogeneous on a wide range of scales from stars, galaxies, through galaxy clusters, up to forming superclusters, filaments, and low-density voids. The propagation of a light ray is therefore influenced by the gravitational field caused by these inhomogeneous mass distributions. The light propagation in an arbitrary curved space time is in general a complicated theoretical problem. However, most of the astrophysical relevant situations allow for a much simpler description of the light ray propagation, which is called the gravitational lensing theory. This section reviews briefly the gravitational lensing theory in order to provide a foundation for later discussions on cluster weak lensing as well as to summarize the basic equations and concepts on cosmological gravitational lensing.

**2.1. Gravitational Deflection and Lens Equation.** – To begin with, let us consider the bending of light rays in the asymptotically flat spacetime caused by a quasi-stationary/spatially-isolated mass distribution, assuming that the gravitational field is weak or the deflection angle is small. This can be done by solving the null geodesic equation in the Minkowski spacetime perturbed with the Newtonian gravitational potential (see, e.g., Ref. [24]). The perturbed metric  $g_{\mu\nu}$  ( $\mu, \nu = 0, 1, \dots, 3$ ) is then written as

$$(1) \quad ds^2 = g_{\mu\nu} dx^\mu dx^\nu = -(1 + 2\Psi/c^2)c^2 dt^2 + (1 + 2\Psi/c^2)^{-1} \delta_{ij} dx^i dx^j,$$

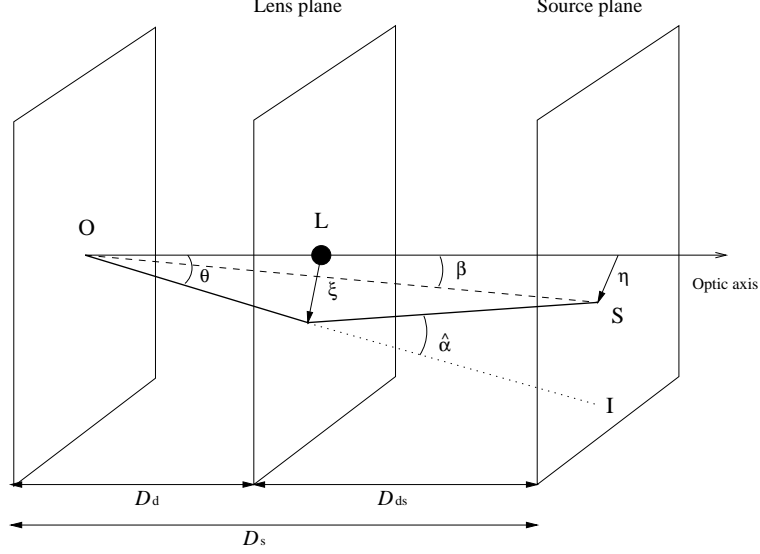


Fig. 1. – Illustration of a gravitational lensing system. The light ray propagates from the source  $S$  at the position  $\eta$  in the source plane to the observer  $O$ , passing the position  $\xi$  in the lens plane where it is deflected by an angle  $\hat{\alpha}$ . The angular position of the source  $S$  relative to the optic axis is denoted by  $\beta$ , and that of the image  $I$  relative to the optical axis is denoted by  $\theta$ . The angular diameter distances between the observer and lens, between the lens and source, and between the observer and source are  $D_d$ ,  $D_{ds}$ , and  $D_s$ , respectively.

where  $\Psi$  is the Newtonian gravitational potential,  $\delta_{ij}$  ( $i, j = 1, 2, 3$ ) is the Kronecker delta, and  $c$  is the speed of light. We consider the metric given by equation (1) to be the sum of a background metric  $g_{\mu\nu}^{(b)}$  and a small perturbation  $h_{\mu\nu}$ :  $g_{\mu\nu} = g_{\mu\nu}^{(b)} + h_{\mu\nu}$  with  $|h_{\mu\nu}| \ll 1$ . Expanding to the first order in  $\Psi/c^2$  we break up the metric in equation (1) into a sum of the background Minkowski metric  $g_{\mu\nu}^{(b)} = \eta_{\mu\nu} = \text{diag}(-1, 1, 1, 1)$  and a perturbation of the form:  $h_{\mu\nu} = \text{diag}(-2\Psi/c^2, -2\Psi/c^2, -2\Psi/c^2, -2\Psi/c^2)$ . As usual,  $g^{\mu\nu}$  and  $g^{(b)\mu\nu}$  are defined by  $g^{\mu\rho}g_{\rho\nu} = \delta_\nu^\mu$  and  $g^{(b)\mu\rho}g_{\rho\nu}^{(b)} = \delta_\nu^\mu$ . Then, to the first order of  $h$ ,  $g^{\mu\nu} = g^{(b)\mu\nu} - h^{\mu\nu}$ , where  $h^{\mu\nu}$  is defined by  $h^{\mu\nu} = g^{(b)\mu\rho}g^{(b)\nu\sigma}h_{\rho\sigma}$ .

The propagation of light rays is described by the null geodesic equation:

$$\begin{aligned}
 (2) \quad k^\mu &\equiv \frac{dx^\mu(\lambda)}{d\lambda}, \\
 (3) \quad 0 &= g_{\mu\nu}k^\mu k^\nu, \\
 (4) \quad \frac{dk^\mu}{d\lambda} &= -\Gamma_{\nu\lambda}^\mu k^\nu k^\lambda,
 \end{aligned}$$

where  $k^\mu$  is the 4-momentum of the light ray,  $\lambda$  is the affine parameter, and  $\Gamma_{\nu\lambda}^\mu$  denotes the Christoffel symbol:  $\Gamma_{\nu\rho}^\mu = (1/2)g^{\mu\lambda}(g_{\lambda\nu,\rho} + g_{\lambda\rho,\nu} - g_{\nu\rho,\lambda})$ . In the background Minkowski spacetime with  $g_{\mu\nu}^{(b)} = \eta_{\mu\nu}$ ,  $\Gamma_{\nu\rho}^{(b)\mu} = 0$ . For a light ray moving into the positive  $x$ -direction in the background spacetime, the photon 4 momentum  $k^{(b)\mu}$  and the corresponding unperturbed orbit  $x^{(b)\mu} = (ct, \mathbf{x})$  are simply given as  $k^{(b)\mu} = dx^{(b)\mu}/d\lambda =$

$(1, 1, 0, 0)$  and  $x^{(b)\mu} = (\lambda, \lambda, 0, 0)$ .

Now we consider the light ray propagation in the perturbed space time. Without loss of generality, we can take the deflection angle to lie in the  $xz$  plane (i.e.,  $y \equiv x^2 = 0$ ). In the weak field limit ( $|\Psi/c^2| \ll 1$ ) the impact parameter  $b$  of the incoming light ray is much greater than the Schwarzschild radius of the deflector,  $b \gg 2GM/c^2$ . The linearized null geodesic equation takes the form:

$$(5) \quad k^\mu(\lambda) = k^{(b)\mu}(\lambda) + \delta k^\mu(\lambda),$$

$$(6) \quad 0 = h_{\mu\nu} k^{(b)\mu} k^{(b)\nu} + 2g_{\mu\nu}^{(b)} k^{(b)\mu} \delta k^\nu,$$

$$(7) \quad \frac{d(\delta k^\mu)}{d\lambda} = -2\Gamma_{\nu\lambda}^{(b)\mu} k^{(b)\nu} \delta k^\lambda - \delta\Gamma_{\nu\lambda}^\mu k^{(b)\nu} k^{(b)\lambda}.$$

Note that the first term on the right-hand side of equation (7) vanishes since  $\Gamma^{(b)} = 0$ . The perturbed Christoffel symbol is  $\delta\Gamma_{\nu\rho}^\mu = (1/2)\eta^{\mu\lambda}(h_{\lambda\nu,\rho} + h_{\lambda\rho,\nu} - h_{\nu\rho,\lambda}) + O(h^2)$ . Choosing the boundary condition  $\delta k^\mu(-\infty) = 0$ , we integrate the linearized geodesic equation (7) to obtain the 4 momentum of the light ray in the *out* state as:

$$(8) \quad \delta k^\mu(+\infty) = \begin{cases} -2 \int_{-\infty}^{+\infty} d\lambda \partial_{||} \Psi / c^2 & (\mu = 0) \\ 0 & (\mu = 1) \\ -2 \int_{-\infty}^{+\infty} d\lambda \partial_{\perp} \Psi / c^2 & (\mu = 2) \end{cases}.$$

In the small angle scattering limit ( $|\Psi/c^2| \ll 1$ ), the bending angle  $\hat{\alpha}$  of the light ray is obtained as

$$(9) \quad \hat{\alpha} \approx \frac{k^{\perp}(+\infty)}{k^{||}(-\infty)} \approx -\frac{2}{c^2} \int_{-\infty}^{+\infty} d\lambda \partial_{\perp} \Psi(\lambda).$$

For  $\mu = 1$  (the  $x^{||}$ -component),  $\delta k^{||}(\lambda) = \text{const.} = 0$ , so that  $k^{||}(\lambda) = 1$  and  $x^{||} = \lambda + O(|h|)$ . This suggests a simple approximation for the bending angle consistent with the weak field limit: Using  $d\lambda = dx^{||} + O(|h|)$  and integrating along the unperturbed path, we have

$$(10) \quad \hat{\alpha} \approx -\frac{2}{c^2} \int_{-\infty}^{+\infty} dx^{||} \nabla_{\perp} \Psi(x^{||}, \mathbf{x}_{\perp}).$$

This is known as the Born approximation. This yields an explicit expression for the bending angle as  $\hat{\alpha} \approx 4GM/(bc^2) \approx 1.75''(M/M_{\odot})(b/R_{\odot})^{-1}$ . General relativity gives a deflection angle twice as large as that Newtonian physics would provide. Eddington confirmed the prediction of general relativity from the measurement of the deflection of the starlight during a solar eclipse. This solar deflection angle is verified within  $\sim 0.1\%$ [29].

Finally, we find from the null condition (equation [3]) that  $\delta k^0(\lambda) = -2\Psi(\lambda) + O(h^2)$ , or  $dt/d\lambda = 1 - 2\Psi(\lambda) + O(h^2) > 1$ . The gravitational time delay  $\Delta t_{\text{grav}}$ , with respect to the unperturbed light propagation, is thus given by

$$(11) \quad c\Delta t_{\text{grav}} = -2 \int_{-\infty}^{+\infty} d\lambda \Psi(\lambda)/c^2.$$

Let us consider a situation as illustrated in Figure 1: A light ray propagates from a source  $S$  at the position  $\boldsymbol{\eta}$  in the source plane to an observer  $O$ , passing the position  $\boldsymbol{\xi}$  in the lens plane where it is deflected by a bending angle  $\hat{\boldsymbol{\alpha}}$ . Here the source and lens planes are defined as planes perpendicular to the optical axis at the distance of the source and the lens, respectively. The exact definition of the optical axis does not matter since the angular scales involved in a typical lensing situation are very small. The angle between the optical axis and the *true* source position is  $\boldsymbol{\beta}$ , and the angle between the optical axis and the image  $I$  is  $\boldsymbol{\theta}$ . The angular diameter distances from the observer to the deflector, from the observer to the source, and from the deflector to the source, are denoted by  $D_d$ ,  $D_s$ , and  $D_{ds}$ , respectively. From Figure 1, we find the following geometrical relation:  $\boldsymbol{\eta} = (D_s/D_d)\boldsymbol{\xi} - D_{ds}\hat{\boldsymbol{\alpha}}(\boldsymbol{\xi})$ . Equivalently, this is transformed to the relation between the angular source and image positions,  $\boldsymbol{\beta} = \boldsymbol{\eta}/D_s$  and  $\boldsymbol{\theta} = \boldsymbol{\xi}/D_d$ :

$$(12) \quad \boldsymbol{\beta} = \boldsymbol{\theta} + \frac{D_{ds}}{D_s}\hat{\boldsymbol{\alpha}}(D_d\boldsymbol{\theta}) \equiv \boldsymbol{\theta} + \boldsymbol{\alpha}(\boldsymbol{\theta}),$$

where we have defined the reduced deflection angle  $\boldsymbol{\alpha}(\boldsymbol{\theta})$  in the last step. Equation (12) is called the *lens equation*, or ray-tracing equation. The lens equation is in general non-linear (with respect to  $\boldsymbol{\theta}$ ), so that it may have several solutions  $\boldsymbol{\theta}$  for a given source position  $\boldsymbol{\beta}$ , corresponding to the multiple imaging of a single source on the sky.

**2.2. Cosmological Lens Equation.** – Here we turn to the cosmological lens equation that describes the light propagation in an expanding, locally-inhomogeneous universe. There are various approaches to derive the cosmological lens equation [30, 31, 32, 33]. Here we follow the approach by Futamase [33] based on the linearized null geodesic equation as introduced in §2.1.

Consider the following perturbation of the Friedman-Lemaitre-Robertson-Walker (FLRW) metric:

$$(13) \quad ds^2 = a^2(\eta)d\tilde{s}^2 \equiv a^2(\eta)\tilde{g}_{\mu\nu}dx^\mu dx^\nu,$$

$$(14) \quad = a^2 \left[ -(1 + 2\Psi)d\eta^2 + (1 - 2\Psi) \{ d\chi^2 + r^2(\chi)(d\theta^2 + \sin^2\theta d\phi^2) \} \right],$$

where  $(x^\mu) = (\eta, \chi, \theta, \phi)$ ,  $\eta = c \int^t dt'/a(t')$  is the conformal time, and  $r(\chi)$  is the comoving angular diameter distance defined by

$$(15) \quad r(\chi) = \begin{cases} K^{-1/2} \sin(\chi/\sqrt{K}) & K > 0 \\ \chi & K = 0 \\ (-K)^{-1/2} \sinh(\chi/\sqrt{-K}) & K < 0 \end{cases}.$$

The curvature parameter  $K$  is expressed with the present-day total density parameter of the Universe  $\Omega_0$  as  $K = (\Omega_0 - 1)H_0^2/c^2$ . Since the structure of a light cone is invariant under the conformal transformation, we work in the conformally-related spacetime with a null geodesic given by  $d\tilde{s}^2$ . The metric  $\tilde{g}_{\mu\nu}$  can be rewritten in the form of  $\tilde{g}_{\mu\nu} = \tilde{g}_{\mu\nu}^{(b)} + h_{\mu\nu}$ , as a sum of the background FLRW metric and a small perturbation ( $|h| \ll 1$ ). The cosmological Poisson equation relates the Newtonian gravitational potential  $\Psi$  to the density perturbation field,  $\delta\rho_m$ , as:

$$(16) \quad \nabla^2\Psi(\boldsymbol{\chi}) = 4\pi G a^2 \delta\rho_m = \frac{3H_0^2\Omega_m}{2} \frac{\delta_m}{a}$$

where  $\delta_m = \delta\rho_m/\bar{\rho}$  is the overdensity with respect to the mean background density of the universe,  $\Omega_m$  is the present-day matter density parameter, and  $\bar{\rho}$  is the mean cosmic matter density,  $\bar{\rho} = \Omega_m a^{-3} \rho_{\text{crit},0} = a^{-3} (3H_0^2 \Omega_m)/(8\pi G)$ . The physical implication of equation (16) is that the amplitude of  $\Psi$  is related to the amplitude of  $\delta$  as  $|\Psi/c^2| \sim (3\Omega_m/2)(l/L_H)^2(\delta_m/a)$  where  $l$  and  $L_H = c/H_0$  denote the characteristic comoving scale of the density fluctuation and the Hubble radius, respectively. Therefore, assuming the standard power spectrum of the density perturbation, we can safely conclude that the degree of metric perturbation is always much smaller than unity, i.e.,  $|\Psi/c^2| \ll 1$ , even for highly non-linear perturbations with  $|\delta_m| \gg 1$  on small scales of  $l \ll L_H (\simeq 3 \text{ Gpc } h^{-1})$ .

Following the prescription given in §2.1, we solve the null geodesic equation (equations [2], [3], [4]) on the perturbed FLRW metric (13). Choosing the origin of the coordinate system at the observer's point and backward ray-tracing from the observer  $\lambda = 0$  to the source  $\lambda = \lambda_s$  along the photon path, we obtain the 4-momentum of the light ray in the background FLRW spacetime as  $k^{(b)\mu} = (-1, 1, 0, 0)$ , and the corresponding orbit as  $x^{(b)\mu}(\lambda) = (-\lambda, \lambda, \theta_I, \phi_I)$  with  $\theta_I \ll 1$ , where  $(\theta_I, \phi_I) = (\theta(0), \phi(0))$  denotes the angular direction of the image on the celestial sphere. The comoving angular diameter distance  $r(\chi)$  defined by equation (15) can be parametrized by the affine parameter along the photon path as  $r(\chi(\lambda)) = r(\lambda)$ . The null geodesic equation for the perturbative part is given by equations (5), (6), (7), and can be formally solved as

$$(17) \quad \delta k^\mu(\lambda) = -\frac{2}{r^2(\lambda)} \int_0^{\lambda_s} d\lambda' \partial^\mu \Psi(\lambda')/c^2 \quad (\mu = \theta, \phi),$$

where  $\partial^\mu \Psi = (\Psi, \sin^{-2} \theta \Psi, \phi)$ . Inserting this in equation (5) and integrating the angular part yields the following equation:

$$(18) \quad \theta_S^\mu \equiv \theta^\mu(\lambda_s) = \theta_I^\mu - \frac{2}{c^2} \int_0^{\lambda_s} d\lambda \frac{r(\lambda_s - \lambda)}{r(\lambda_s)r(\lambda)} \partial^\mu \Psi(\lambda),$$

where quantities with the subscript  $S$  denote those defined for the source. Now we consider a small patch of the sky over which the curvature of the sky is negligible (flat-sky approximation). Then, one can define locally flat-sky Cartesian coordinates  $\boldsymbol{\theta} = (\theta, \theta\phi)$  around the line-of-sight of interest ( $\theta \ll 1$ ). Defining  $\boldsymbol{\beta} \equiv \boldsymbol{\theta}_S$  and  $\boldsymbol{\theta} \equiv \boldsymbol{\theta}_I$ , equation (18) is written in this coordinate system as

$$(19) \quad \boldsymbol{\beta} - \boldsymbol{\theta} = \int_{\text{Observer}}^{\text{Source}} d\boldsymbol{\alpha} = \boldsymbol{\alpha}(\chi_s),$$

$$(20) \quad \boldsymbol{\alpha}(\chi_s) = -\frac{2}{c^2} \int_0^{\lambda_s} d\lambda \frac{r(\lambda_s - \lambda)}{r(\lambda_s)} \boldsymbol{\nabla}_\perp \Psi(x(\lambda)); \quad x(\lambda) = x^{(b)}(\lambda) + \delta x(\lambda),$$

where  $\boldsymbol{\nabla}_\perp$  is the (comoving) transverse derivative,  $\boldsymbol{\nabla}_\perp \equiv r^{-1}(\lambda)(\partial_\theta, \theta^{-1}\partial_\phi)$ , and the integral is performed along the perturbed trajectory  $x(\lambda) = x^{(b)}(\lambda) + \delta x(\lambda)$  with  $\lambda = \chi + O(|\Psi/c^2|)$ . This is a general expression of the cosmological lens equation: as long as the approximations adopted are valid (see Refs. [33] and [34] for more details), equation (19) can be applied to various lensing phenomena, including the multiple deflections of light rays, strong and weak lensing by clusters of galaxies, and the weak lensing by the cosmic large-scale structure continuously distributed between the source and the observer. Note that the cosmological lens equation (19) is derived with the standard angular diameter distance in FLRW spacetime *without* employing the thin lens approximation.

**2.3. Cluster Gravitational Lensing.** – Now, let us turn to the case of gravitational lensing by clusters of galaxies. Clusters are the largest gravitationally-bound systems observed in the Universe, with typical masses of  $M \sim 10^{14} - 10^{15} M_\odot$ . In the context of the standard structure formation scenario, clusters, as the most massive collapsed structures, correspond to rare peaks in the primordial density field. Clusters produce deep gravitational potential wells, and act as efficient gravitational lenses. The large-scale structure in the Universe also affects the propagation of light rays from distant sources, producing small but continuous transverse excursions of light rays along the light path. In the study of cluster gravitational lensing, it is often assumed that the total deflection angle  $\alpha$  is dominated by the gravitational potential of the cluster itself, and that contributions from the cosmic large-scale structure and multiple deflections by other non-linear objects are negligible. Assuming that the light propagation is approximated by a single scattering event by the cluster (single lens approximation) and that a light deflection occurs within a sufficiently small region ( $\chi_d - \Delta\chi/2, \chi_d + \Delta\chi/2$ ) compared to the relevant angular diameter distances (thin-lens approximation), we have the deflection angle by a single cluster as

$$(21) \quad \alpha(\theta) \approx -\frac{2}{c^2} \frac{D_{ds}}{D_s} \int_{\chi_d - \Delta\chi/2}^{\chi_d + \Delta\chi/2} d\chi \nabla_\perp \Psi(\chi, r(\chi_d)\theta),$$

where  $D_s = a(\chi_s)r(\chi_s)$  and  $D_{ds} = a(\chi_s)r(\chi_s - \chi_d)$  are the angular diameter distances from the observer to the source, and from the deflector to the source, respectively, and  $r(\chi_d)\theta$  is the comoving transverse vector on the lens plane. In a cosmological situation, the angular diameter distances  $D_{ij}$  between the planes  $i$  and  $j$  ( $z_i < z_j$ ) are of the order of the Hubble radius,  $L_H \equiv c/H_0 \approx 3 \text{ Gpc } h^{-1}$ , while physical extents of clusters are about  $2R = 2 - 5 \text{ Mpc } h^{-1}$ . Therefore, one can safely adopt the thin-lens approximation in cluster gravitational lensing.

In actual observations, large scale structure along the line-of-sight also contributes to the lensing signal, and consequently affects the measurements of cluster mass properties. The level of uncertainties on cluster lensing measurements due to large scale structure can be assessed by numerical simulations (see Ref. [35]). For a massive cold dark matter (CDM) halo with  $M_{200} = 10^{15} M_\odot h^{-1}$ , uncertainties in the mass measurement could reach 16 – 18% at intermediate redshifts of  $z_d = 0.2 - 0.3$ [35]. See also Appendix A for the multiple lens equation based on a discretized version of the cosmological lens equation.

Then, we introduce the *effective lensing potential*  $\psi(\theta)$  defined as

$$(22) \quad \psi(\theta) \approx \frac{2}{c^2} \frac{D_{ds}}{D_d D_s} \int_{\chi_d - \Delta\chi/2}^{\chi_d + \Delta\chi/2} \Psi(\chi, r(\chi_d)\theta) d\chi,$$

where  $D_d$  is the angular diameter distance from the observer to the deflector,  $D_d = a(\chi_d)r(\chi_d)$ . In terms of  $\psi(\theta)$ , the lens equation is expressed as

$$(23) \quad \beta = \theta - \nabla_\theta \psi(\theta); \quad \alpha(\theta) = -\nabla_\theta \psi(\theta),$$

where  $\nabla_\theta = r \nabla_\perp = (\partial_\theta, \theta^{-1} \partial_\phi)$ . Table 1 gives examples of analytic axially-symmetric lens models based on spherically-symmetric mass distributions, such as the point mass,

TABLE I. – Examples of analytic lens models based on the spherical symmetric mass distribution. The 3D density profile  $\rho(r)$ , the lensing convergence  $\kappa(\theta)$ , and the mean convergence  $\bar{\kappa}(\theta)$  inside the angular radius  $\theta$  are given. Here ‘T’ and ‘R’ indicates that the lens has a tangential and a radial critical curve, respectively.

Model	$\rho(r)$	$\kappa(\theta)$	$\bar{\kappa}(\theta)$	Remarks
Point mass	$M\delta_D^3(\vec{r})$	$\frac{4\pi GM}{c^2} \frac{D_d D_{ds}}{D_s} \delta_D^2(\vec{\theta})$	$\frac{4GM}{c^2} \frac{D_d D_{ds}}{D_s} \frac{1}{\theta^2}$	T
SIS <sup>(1)</sup>	$\frac{\sigma_v^2}{2\pi G r^2}$	$2\pi G \left(\frac{\sigma_v}{c}\right)^2 \frac{D_{ds}}{D_s} \frac{1}{\theta}$	$4\pi G \left(\frac{\sigma_v}{c}\right)^2 \frac{D_{ds}}{D_s} \frac{1}{\theta}$	T
ISC <sup>(2)</sup>	$\frac{\rho(0)}{1 + (r/r_c)^2}$	$\frac{\kappa(0)}{\sqrt{1 + (\theta/\theta_c)^2}}$	$2\kappa(0) \frac{\sqrt{1 + (\theta/\theta_c)^2} - 1}{(\theta/\theta_c)^2}$	T, R
NFW <sup>(3)</sup>	$\frac{\rho_{\text{crit}} \delta_c}{(r/r_s)(1 + r/r_s)^2}$	$\kappa_s f(\theta/\theta_s)$	$2\kappa_s g(\theta/\theta_s)/(\theta/\theta_s)^2$	T, R

Notes.

(1) Singular isothermal sphere:  $\sigma_v$  represents the isothermal 1D velocity dispersion.

(2) Isothermal sphere with a finite core radius:  $r_c$  represents the core radius, and  $\theta_c$  is its angular radius,  $\theta_c := r_c/D_d$ ;  $\kappa(0) := \Sigma_m(0)/\Sigma_{\text{crit}}$  with  $\Sigma_m(0) = \pi\rho(0)r_c$ . The ISC produces two critical curves if, and only if,  $\kappa(0) > 1$ .

(3) Navarro, Frenk, and White (NFW[37]) universal profile of cold dark matter (CDM) halos:  $\delta_c$ ,  $\rho_{\text{crit}}$ , and  $r_s$  represent the characteristic overdensity of the CDM halo, the critical density of the Universe, and the scale radius, respectively.  $\kappa_s$  and  $\theta_s$  are then defined by  $\kappa_s := 2\delta_c\rho_{\text{crit}}r_s\Sigma_{\text{crit}}^{-1}$  and  $\theta_s := r_s/D_d$ , respectively. The functions  $f(x)$  and  $g(x)$  are defined as follows[38][39]:

$$(24) \quad f(x) = \begin{cases} \frac{1}{1-x^2} \left( -1 + \frac{2}{\sqrt{1-x^2}} \operatorname{arctanh} \sqrt{\frac{1-x}{1+x}} \right) & (x < 1) \\ \frac{1}{3} & (x = 1); \\ \frac{1}{x^2-1} \left( +1 - \frac{2}{\sqrt{x^2-1}} \arctan \sqrt{\frac{x-1}{x+1}} \right) & (x > 1) \end{cases}$$

$$(25) \quad g(x) = \ln\left(\frac{x}{2}\right) + \begin{cases} \frac{2}{\sqrt{1-x^2}} \operatorname{arctanh} \sqrt{\frac{1-x}{1+x}} & (x < 1) \\ 1 & (x = 1). \\ \frac{2}{\sqrt{x^2-1}} \arctan \sqrt{\frac{x-1}{x+1}} & (x > 1) \end{cases}$$

the singular isothermal sphere, and the NFW models. For a more complete *catalog* of mass models for gravitational lensing, see Keeton [36].

**2.4. Lensing Jacobian Matrix.** – The local properties of the lens mapping are described by the Jacobian matrix  $\mathcal{A}$ :

$$(26) \quad \mathcal{A}(\boldsymbol{\theta}) = \left( \frac{\partial \boldsymbol{\beta}}{\partial \boldsymbol{\theta}} \right) = \begin{pmatrix} 1 - \psi_{,11} & -\psi_{,12} \\ -\psi_{,12} & 1 - \psi_{,22} \end{pmatrix}.$$



This symmetric  $2 \times 2$  Jacobian matrix can be decomposed into the following form:

$$(27) \quad \mathcal{A}_{\alpha\beta} = \delta_{\alpha\beta} - \psi_{,\alpha\beta} = (1 - \kappa)\delta_{\alpha\beta} - \gamma_1\sigma_3 - \gamma_2\sigma_1$$

where  $\kappa(\boldsymbol{\theta})$  is the lensing convergence field defined by

$$(28) \quad \kappa = \frac{1}{2}(\psi_{,11} + \psi_{,22}) = \frac{1}{2}\Delta_{\theta}\psi(\boldsymbol{\theta}),$$

responsible for the trace-part of the Jacobian matrix,  $\gamma_{\alpha}(\boldsymbol{\theta})$  ( $\alpha = 1, 2$ ) are the components of the complex shear field  $\gamma(\boldsymbol{\theta}) := \gamma_1(\boldsymbol{\theta}) + i\gamma_2(\boldsymbol{\theta})$ , defined as

$$(29) \quad \gamma_1 = \frac{1}{2}(\psi_{,11} - \psi_{,22}); \quad \gamma_2 = \frac{1}{2}(\psi_{,12} + \psi_{,21}) = \psi_{,12},$$

and  $\sigma_a$  ( $a = 1, 2, 3$ ) are the Pauli matrices that satisfy  $\sigma_a\sigma_b = i\epsilon_{abc}\sigma_c$ . Equation (28) can be regarded as the two-dimensional Poisson equation. Then, the Green's function (or the propagator) in the infinite domain ( $\mathcal{R}^2$ ) is  $\Delta^{-1}(\boldsymbol{\theta}, \boldsymbol{\theta}') = \ln|\boldsymbol{\theta} - \boldsymbol{\theta}'|/(2\pi)$ , so that  $\psi(\boldsymbol{\theta}) = (1/\pi)\int_{\mathcal{R}^2}d^2\theta' \ln(\boldsymbol{\theta} - \boldsymbol{\theta}')\kappa(\boldsymbol{\theta}')$ . The explicit representation of the lens Jacobian matrix is

$$(30) \quad \mathcal{A}(\boldsymbol{\theta}) = \begin{pmatrix} 1 - \kappa - \gamma_1 & -\gamma_2 \\ -\gamma_2 & 1 - \kappa + \gamma_1 \end{pmatrix} = (1 - \kappa) \begin{pmatrix} 1 & 0 \\ 0 & 1 \end{pmatrix} - \begin{pmatrix} \gamma_1 & \gamma_2 \\ \gamma_2 & -\gamma_1 \end{pmatrix},$$

and it has two eigenvalues  $\Lambda_{\pm} = 1 - \kappa \pm |\gamma|$ . In Figure 2 we illustrate the effects of the lensing convergence  $\kappa$  and the gravitational shear  $\gamma$  on the shape and size of an infinitesimal circular source.

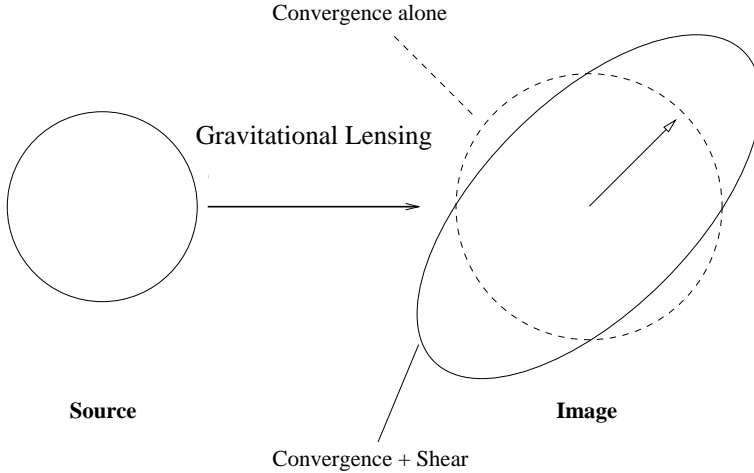


Fig. 2. – Illustration of the effects of the convergence  $\kappa$  and the shear  $\gamma$  on the shape and size of a hypothetical circular source. The convergence acting alone causes an isotropic magnification of the image (dashed circle), while the shear deforms it to an ellipse.

**2'5. Lensing Convergence.** – The lensing convergence  $\kappa$  is essentially a distance weighted mass overdensity projected along the line-of-sight. We express  $\kappa(\boldsymbol{\theta})$  due to cluster gravitational lensing as

$$(31) \quad \kappa(\boldsymbol{\theta}) = \int dl (\rho_m - \bar{\rho}) \left( \frac{c^2}{4\pi G} \frac{D_s}{D_s D_{ds}} \right)^{-1} \simeq \frac{\Sigma_m(\boldsymbol{\theta})}{\Sigma_{\text{crit}}}; \quad dl = ad\chi,$$

where  $\Sigma_m = \int dl (\rho_m - \bar{\rho}) \approx \int dl \rho_m$  is the surface mass density field of the lensing cluster projected on the sky, and  $\Sigma_{\text{crit}}$  is the critical surface mass density of gravitational lensing,

$$(32) \quad \Sigma_{\text{crit}} = \frac{c^2}{4\pi G} \frac{D_s}{D_s D_{ds}} \simeq 0.1 h \text{ g/cm}^2 \left( \frac{\tilde{d}_s}{\tilde{d}_d \tilde{d}_{ds}} \right),$$

where  $\tilde{d}_{ij} \equiv D_{ij}/L_H$  is the dimensionless angular diameter distance between the planes  $i$  and  $j$ ;  $\Sigma_{\text{crit}}$  depends on the lensing geometry  $(z_d, z_s)$  and the geometry of the Universe, e.g.,  $(\Omega_m, \Omega_\Lambda, H_0)$ .

For a given lens redshift  $z_d$ , the geometric efficiency of gravitational lensing is determined by the distance ratio,  $D_{ds}/D_s$ , given as a function of the background redshift  $z_s$  and the cosmological parameters. Figure 3 compares  $D_{ds}/D_s$  as a function of  $z_s$  for various sets of the lens redshift and the cosmological model. In order to convert the observed lensing signal into physical mass units, one needs to evaluate the depth of background sources (i.e., the source redshift distribution, or its moments). Figure 4 shows  $\Sigma_{\text{crit}}^{-1} \propto D_{ds}/D_s$  as a function of lens redshift  $z_d$  for three different source redshifts,  $z_s = 0.8, 1.0, 1.2$ . In typical optical imaging observations down to a magnitude limit of  $R_c \sim 26$  ABmag, the median depth of background galaxies is about  $z_s \sim 1$ . When the lens redshift is  $z_d \lesssim 0.2$ ,  $\Sigma_{\text{crit}}$  depends weakly on the source redshift, so that a precise knowledge of the redshift distribution of background galaxies is not crucial (see for details, e.g. Refs. [40] and [13]). On the other hand, this distance dependence of the lensing effects can be used to constrain the cosmological redshift-distance relation by examining the geometric scaling of the lensing signal as a function of the background redshift (see Refs. [41] and [42]).

**2'6. Quadrupole Shape Distortion: Gravitational Shear.** – The deformation of the image for an infinitesimally small background source ( $d\boldsymbol{\beta} \rightarrow 0$ ) can be described by the inverse Jacobian matrix  $\mathcal{A}_{\alpha\beta}^{-1} \equiv (\mathcal{A}^{-1})_{\alpha\beta}$  of the lens equation  $(\alpha, \beta = 1, 2)$ . In the weak lensing limit,

$$(33) \quad \mathcal{A}_{\alpha\beta}^{-1} \approx (1 + \kappa)\delta_{\alpha\beta} + \Gamma_{\alpha\beta},$$

where

$$(34) \quad \Gamma_{\alpha\beta} \equiv \left( \partial_\alpha \partial_\beta - \delta_{\alpha\beta} \frac{1}{2} \Delta_\theta \right) \psi(\boldsymbol{\theta}) = \sigma_3 \gamma_1 + \sigma_1 \gamma_2$$

is the symmetric, trace-free  $2 \times 2$  shear tensor[4][43]. The first term in equation (33) describes the isotropic light focusing (area distortion) in the weak lensing limit, while the second term induces an asymmetry in lens mapping; the shear is hence responsible for the shape distortion. Note that both the convergence and the shear contribute to the shape/area distortions in general (non-weak) cases.

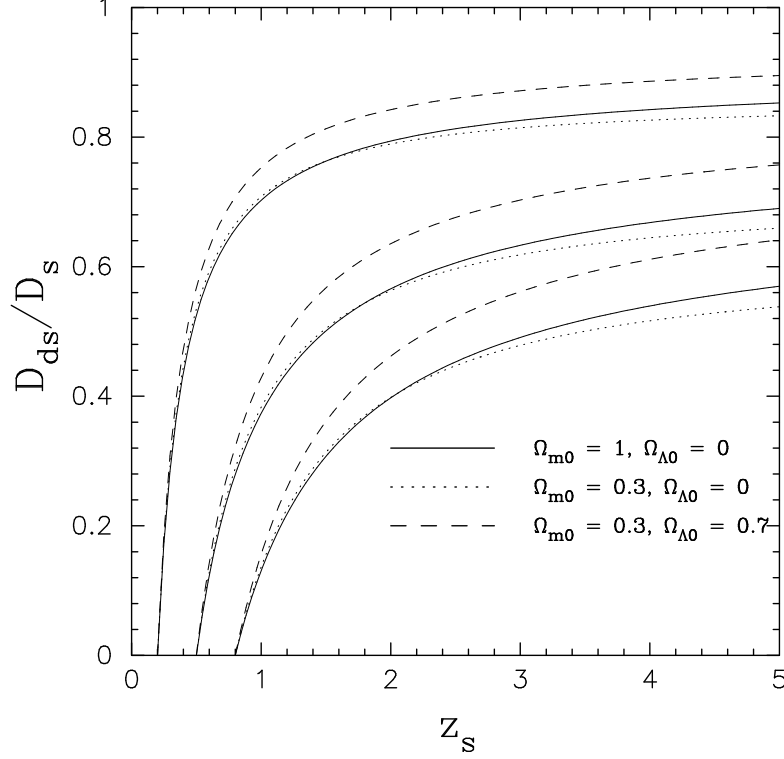


Fig. 3. – Distance ratio  $D_{ds}/D_s$  as a function of the source redshift  $z_s$  for various sets of the lens redshift  $z_d$  and the cosmological parameters  $(\Omega_m, \Omega_\Lambda)$ .  $D_{ds}/D_s$  is plotted for three lens redshifts  $z_d = 0.2, 0.5, 0.8$  (from left to right), and for three sets of the cosmological parameters:  $(\Omega_m, \Omega_\Lambda) = (1, 0), (0.3, 0)$ , and  $(0.3, 0.7)$ .

**2.7. Area Distortion: Gravitational Magnification.** – The determinant of the Jacobian matrix is given as  $\det A = (1 - \kappa)^2 - |\gamma|^2$ . In the weak lensing limit where  $|\kappa|, |\gamma_1|, |\gamma_2| \ll 1$ ,  $\det A \approx 1 - 2\kappa$ . Gravitational lensing describes the light ray deflection in the weak field limit ( $|\Psi/c^2| \ll 1$ ). The surface brightness of a background source is unchanged under gravitational lensing (Liouville's theorem). The flux magnification in gravitational lensing is due to the light-ray focusing that causes the area distortion:  $\delta\Omega^I = \mu\delta\Omega^S$ . The magnification is hence given by taking the ratio between the lensed to the unlensed image solid angle as  $\mu = \delta\Omega^I/\delta\Omega^S = 1/\det A$ :

$$(35) \quad \mu = \frac{1}{\det A} = \frac{1}{(1 - \kappa)^2 - |\gamma|^2}.$$

In the weak lensing limit, the magnification to the first order is

$$(36) \quad \mu \approx 1 + 2\kappa.$$

Thus, for an image at  $\kappa(\theta) = 0.1$ , the corresponding magnitude change is  $\Delta m \approx -(5/2) \log_{10}(\mu) \simeq -0.20$ .

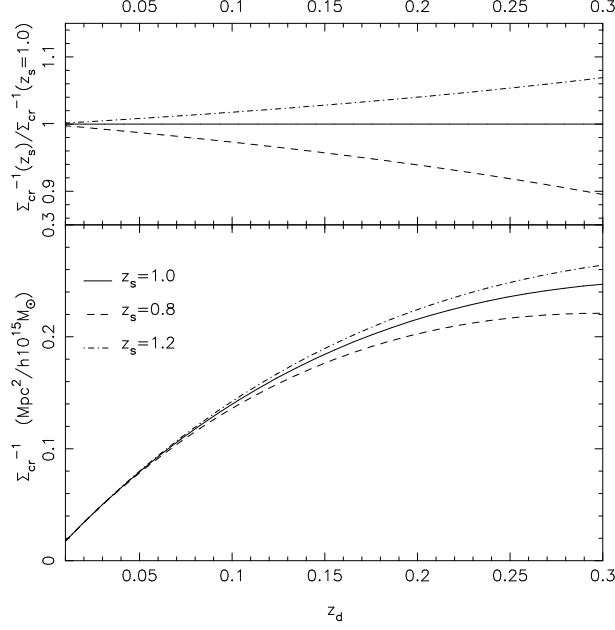


Fig. 4. – Geometric scaling of the weak lensing signal. The lower panel shows the inverse of the critical surface mass density of gravitational lensing,  $\Sigma_{\text{crit}}^{-1}(z_d, z_s)$ , as a function of lens redshift  $z_d$  for three different source redshifts,  $z_s = 0.8, 1.0, 1.2$  (*dashed, solid, and dotted-dashed*, respectively), demonstrating the geometric scaling of gravitational lensing signal. The top panel shows the relative lensing strength  $\Sigma_{\text{crit}}^{-1}(z_d, z_s) / \Sigma_{\text{crit}}^{-1}(z_d, z_s = 1.0)$  as a function of lens redshift  $z_d$  normalized with respect to the source at  $z_s = 1.0$ . For lensing clusters at low redshifts  $z_d$ ,  $\Sigma_{\text{crit}}$  depends very weakly on the background redshift  $z_s$ , so that the uncertainty in  $z_s$  of background galaxies is less important in the lensing-based cluster mass determination. This figure is taken from Ref. [7].

### 3. – Weak Gravitational Lensing

In this section, we assume for simplicity that the lensing fields are subcritical everywhere, i.e.,  $\det \mathcal{A}(\boldsymbol{\theta}) > 0$ .

**3.1. Weak Lensing Mass Reconstruction.** – For convenience we define the complex gradient operator  $\partial := \partial_1 + i\partial_2$  that transforms as a vector,  $\partial' = \partial e^{i\varphi}$ , with  $\varphi$  being the angle of rotation relative to the original basis[44, 45, 46]. In terms of the effective lensing potential  $\psi(\boldsymbol{\theta})$ , the lensing convergence is given as

$$(37) \quad \kappa(\boldsymbol{\theta}) = \frac{1}{2} \partial^* \partial \psi(\boldsymbol{\theta}),$$

where  $*$  denotes the complex conjugate, and  $\partial \partial^* = \nabla_{\boldsymbol{\theta}}^2$  is a scalar or a spin-0 operator. Similarly, the complex shear  $\gamma = \gamma_1 + i\gamma_2 \equiv |\gamma| e^{2i\phi}$  is given as

$$(38) \quad \gamma(\boldsymbol{\theta}) = \frac{1}{2} \partial \partial \psi(\boldsymbol{\theta}) \equiv \hat{\mathcal{D}}_{\boldsymbol{\theta}} \psi(\boldsymbol{\theta}),$$

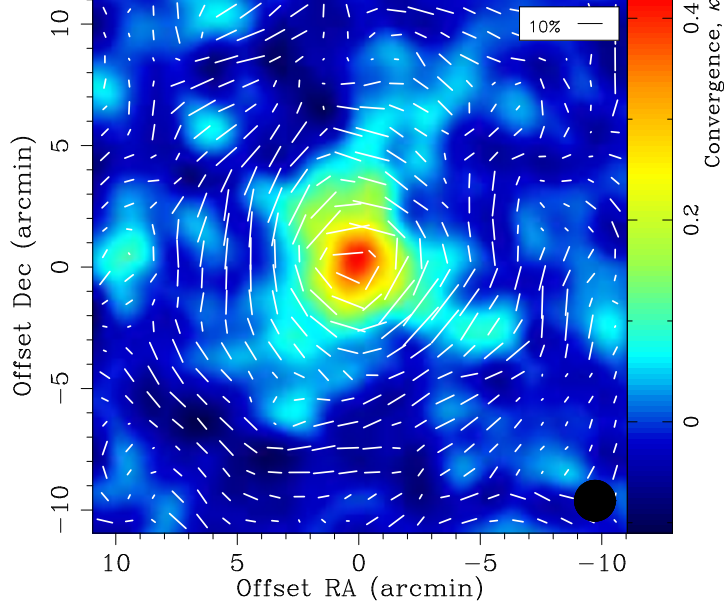


Fig. 5. – The projected mass distribution  $\kappa(\boldsymbol{\theta})$  of A1689 reconstructed using the weak gravitational shear field  $\gamma(\boldsymbol{\theta})$  measured from a color/magnitude-selected sample of red background galaxies registered in deep Subaru imaging observations. Overlaid up on the image is the reconstructed spin-2 gravitational shear field  $\gamma(\boldsymbol{\theta})$ . A stick with the length of 10% shear is indicated in the top right corner. The north is to the top, and the east is to the left. This figure is based on the Subaru weak lensing data presented in Ref. [9].

where  $\hat{\mathcal{D}}_\theta = \partial\partial/2 = (\partial_1^2 - \partial_2^2)/2 + i\partial_1\partial_2$  is a spin-2 operator, which transforms as  $\hat{\mathcal{D}}'_\theta = \hat{\mathcal{D}}_\theta e^{2i\varphi}$  under a rotation of the basis axis by  $\varphi$ .

Since the  $\gamma$ - and  $\kappa$ -fields are linear combinations of the second derivatives of  $\psi(\boldsymbol{\theta})$ ,  $\gamma(\boldsymbol{\theta})$  and  $\kappa(\boldsymbol{\theta})$  are related with each other by (see Refs. [47] and [43]) <sup>(1)</sup>

$$(39) \quad \Delta_\theta \kappa(\boldsymbol{\theta}) = \partial^* \partial^* \gamma = 2\hat{\mathcal{D}}_\theta^* \gamma(\boldsymbol{\theta})$$

Thus, the shear-to-mass inversion formula can be formally obtained as

$$(40) \quad \kappa(\boldsymbol{\theta}) = \Delta_{\theta\theta'}^{-1} [\partial^* \partial^* \gamma(\boldsymbol{\theta}')] = 2\hat{\mathcal{D}}_\theta^* \Delta_{\theta\theta'}^{-1} [\gamma(\boldsymbol{\theta}')].$$

For the two-dimensional Poisson equation, the Green's function (propagator)  $\Delta^{-1}(\boldsymbol{\theta}, \boldsymbol{\theta}')$  in the infinite domain ( $\mathcal{R}^2$ ) is  $\Delta^{-1}(\boldsymbol{\theta}, \boldsymbol{\theta}') = \ln |\boldsymbol{\theta} - \boldsymbol{\theta}'|/(2\pi)$ , so that equation (40) can be solved to yield the following non-local relation between  $\kappa$  and  $\gamma$  (see Ref. [2]):

$$(41) \quad \kappa(\boldsymbol{\theta}) = \frac{1}{\pi} \int_{\mathcal{R}^2} d^2\theta' D^*(\boldsymbol{\theta} - \boldsymbol{\theta}') \gamma(\boldsymbol{\theta}'),$$

---

<sup>(1)</sup> An alternative but equivalent expression is  $\Delta_\theta \kappa(\boldsymbol{\theta}) = \partial^\alpha \partial^\beta \Gamma_{\alpha\beta}(\boldsymbol{\theta})$ .

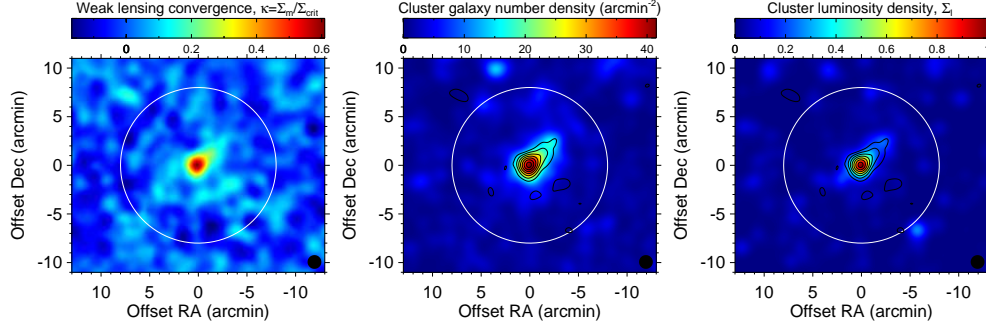


Fig. 6. – Comparison of the surface mass density field and the cluster galaxy distributions in Cl0024+1654. *Left*: Dimensionless surface mass density field, or the lensing convergence  $\kappa(\boldsymbol{\theta}) = \Sigma_m(\boldsymbol{\theta})/\Sigma_{\text{crit}}$ , reconstructed from Subaru distortion data. *Middle*: Observed surface number density distribution  $\Sigma_n(\boldsymbol{\theta})$  of  $BR_c z'$ -selected green galaxies, representing unlensed cluster member galaxies. *Right*: Observed  $R_c$ -band surface luminosity density distribution  $\Sigma_l(\boldsymbol{\theta})$  of the same cluster membership. The solid circle in each panel indicates the cluster virial radius of  $r_{\text{vir}} \simeq 1.8 \text{ Mpc } h^{-1}$  at the cluster redshift of  $z = 0.395$ . All images are smoothed with a circular Gaussian of FWHM 1.4 arcmin. Also overlaid on the  $\Sigma_n(\boldsymbol{\theta})$  and  $\Sigma_l(\boldsymbol{\theta})$  maps are the  $\kappa(\boldsymbol{\theta})$  field shown in the left panel, given in units of  $2\sigma$  reconstruction error from the lowest contour level of  $3\sigma$ . The field size is  $26' \times 22'$ . North is to the top, east to the left. Figure taken from Ref. [40].

where  $D(\boldsymbol{\theta})$  is the complex kernel defined as

$$(42) \quad D(\boldsymbol{\theta}) \equiv 2\pi \hat{D}_\theta \Delta^{-1}(\boldsymbol{\theta}) = \frac{\theta_2^2 - \theta_1^2 - 2i\theta_1\theta_2}{|\boldsymbol{\theta}|^4} = -\frac{1}{(\theta_1 - i\theta_2)^2}.$$

Similarly, the complex shear field can be expressed in terms of the lensing convergence as

$$(43) \quad \gamma(\boldsymbol{\theta}) = \frac{1}{\pi} \int_{\mathcal{R}^2} d^2\theta' D(\boldsymbol{\theta} - \boldsymbol{\theta}') \kappa(\boldsymbol{\theta}').$$

In a practical application, it is computationally fast to work in Fourier domain[48], by using the fast Fourier transform (FFT). By taking the Fourier transform of equation (39), we have a mass inversion relation in Fourier space as

$$(44) \quad \hat{\kappa}(\mathbf{k}) = \frac{k_1^2 - k_2^2 - 2ik_1k_2}{k_1^2 + k_2^2} \hat{\gamma}(\mathbf{k}) \quad (\mathbf{k} \neq 0)$$

where  $\hat{\kappa}(\mathbf{k})$  and  $\hat{\gamma}(\mathbf{k})$  are the Fourier transform of the  $\kappa(\boldsymbol{\theta})$  and  $\gamma(\boldsymbol{\theta}) = \gamma_1(\boldsymbol{\theta}) + i\gamma_2(\boldsymbol{\theta})$  fields, respectively.

Figure 5 shows the two-dimensional mass distribution in the central  $22' \times 22'$  region of A1689 at  $z_d = 0.183$  reconstructed from the weak shear field[9], measured from a sample of blue+red background galaxies registered in deep  $Vi'$  images taken with the Suprime-Cam[49] on the Subaru telescope. Also overlaid up on the image is the gravitational shear field  $\gamma(\boldsymbol{\theta})$  of the red background galaxies, revealing a coherent tangential pattern around the cluster center. In the left panel of Figure 6 we show the mass map for

CL0024+1654 ( $z_d = 0.395$ ) reconstructed from Subaru distortion data of  $BR_c z'$ -selected blue+red background galaxies. Also compared in Figure 6 are member galaxy distributions  $\Sigma_n(\boldsymbol{\theta})$  and  $\Sigma_l(\boldsymbol{\theta})$  in the cluster, Gaussian smoothed to the same resolution of  $\text{FWHM} = 1.41$  arcmin. Overall, mass and light are similarly distributed in the cluster.

Adding a constant mass sheet to  $\kappa$  in equation (43) does not change the shear field  $\gamma(\boldsymbol{\theta})$  which is observable in the weak lensing limit, leading to the so-called *mass-sheet degeneracy* based solely on shape-distortion measurements[4, 5]. As we shall see in §3.2, the observable quantity is not the gravitational shear  $\gamma$  but the *reduced* shear,

$$(45) \quad g(\boldsymbol{\theta}) = \frac{\gamma(\boldsymbol{\theta})}{1 - \kappa(\boldsymbol{\theta})}$$

in the subcritical regime where  $\det \mathcal{A} > 0$  (or  $1/g^*$  in the negative parity region with  $\det \mathcal{A} < 0$ ). We see that the  $g$ -field is invariant under the following global transformation:

$$(46) \quad \kappa(\boldsymbol{\theta}) \rightarrow \lambda \kappa(\boldsymbol{\theta}) + 1 - \lambda, \quad \gamma(\boldsymbol{\theta}) \rightarrow \lambda \gamma(\boldsymbol{\theta})$$

with an arbitrary scalar constant  $\lambda \neq 0$ [3]. This transformation is equivalent to scaling the Jacobian matrix  $\mathcal{A}(\boldsymbol{\theta})$  with  $\lambda$ ,  $\mathcal{A}(\boldsymbol{\theta}) \rightarrow \lambda \mathcal{A}(\boldsymbol{\theta})$ . This mass-sheet degeneracy can be unambiguously broken by measuring the magnification effects, because the magnification  $\mu$  transforms under the invariance transformation (46) as

$$(47) \quad \mu(\boldsymbol{\theta}) \rightarrow \lambda^2 \mu(\boldsymbol{\theta}).$$

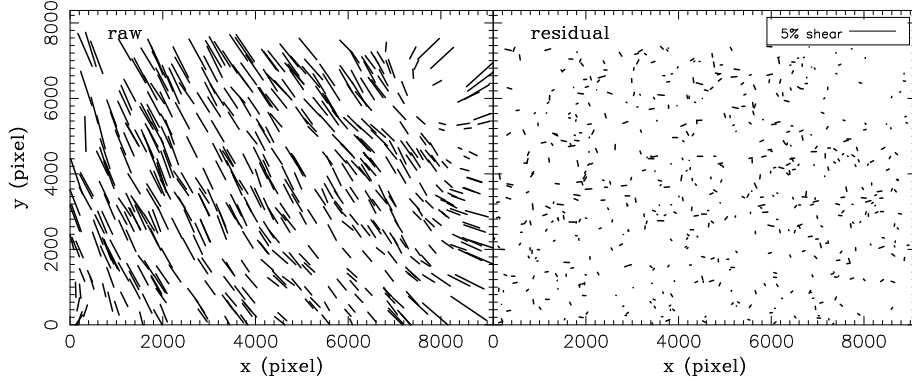


Fig. 7. – Example of the anisotropy point-spread function (PSF) correction (Subaru  $i'$  data of A1689). The quadrupole PSF anisotropy field as measured from stellar ellipticities before and after the PSF anisotropy correction. The left panel shows the raw ellipticity field of stellar objects, and the right panel shows the residual ellipticity field after the PSF anisotropy correction. The orientation of the sticks indicates the position angle of the major axis of stellar ellipticity, whereas the length is proportional to the modulus of stellar ellipticity. A stick with the length of 5% ellipticity is indicated in the top right of the right panel. This figure is taken from Ref. [9].

**3.2. Weak Lensing Distortion Observables.** – In a moment-based approach of weak lensing shape measurements (see Kaiser, Squires, & Broadhurst[50]; hereafter KSB) we

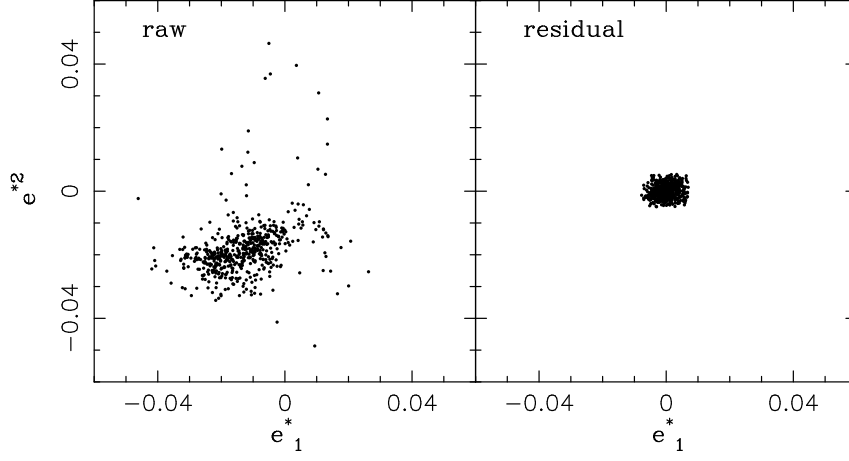


Fig. 8. – Stellar ellipticity distributions before and after the PSF anisotropy correction, corresponding to Figure 7. The left panel shows the raw ellipticity components  $(e_1^*, e_2^*)$  of stellar objects, and the right panel shows the residual ellipticity components  $(\delta e_1^*, \delta e_2^*)$  after the PSF anisotropy correction. This figure is taken from Ref. [9].

use quadrupole moments  $Q_{\alpha\beta}$  ( $\alpha, \beta = 1, 2$ ) of the surface brightness distribution  $I(\boldsymbol{\theta})$  of background images for quantifying the shape of the images:

$$(48) \quad Q_{\alpha\beta} \equiv \frac{\int d^2\theta q_I[I(\boldsymbol{\theta})] \Delta\theta_\alpha \Delta\theta_\beta}{\int d^2\theta q_I[I(\boldsymbol{\theta})]},$$

where  $q_I[I(\boldsymbol{\theta})]$  denotes the weight function used in noisy shape measurements and  $\Delta\theta_\alpha = \theta_\alpha - \bar{\theta}_\alpha$  is the offset vector from the image centroid.<sup>(2)</sup> The complex ellipticity  $e$  is then defined as

$$(49) \quad e \equiv \frac{Q_{11} - Q_{22} + 2iQ_{12}}{Q_{11} + Q_{22}},$$

The spin-2 ellipticity  $e$  transforms under the lens mapping as

$$(50) \quad e^{(s)} = \frac{e - 2g + g^2 e^*}{1 + |g|^2 - 2\text{Re}[ge^*]},$$

where quantities with subscript “(s)” represent those of (unlensed) intrinsic background sources, and  $g = \gamma/(1 - \kappa)$  is the spin-2 reduced shear. Since  $e$  is a non-zero spin quantity with a direction dependence, the expectation value of the intrinsic source ellipticity  $e^{(s)}$  is assumed to vanish:  $\langle e^{(s)} \rangle = 0$ . Schneider & Seitz[3] showed that  $0 = \langle \chi^{(s)} \rangle$  is equivalent

---

<sup>(2)</sup> A practical implementation of the KSB method is achieved by the IMCAT package developed by Nick Kaiser. Note that IMCAT measures the shape moments with respect to the peak position rather than the centroid.



to

$$(51) \quad 0 = \sum_j w_j \frac{e_j - \delta_g}{1 - \Re(\delta_g e_j^*)},$$

where  $\delta_g$  is the spin-2 complex distortion  $\delta_g = 2g/(1+|g|^2)$ [3],  $e_j$  is the complex ellipticity for the  $j$ th object, and  $w_j$  is a statistical weight for the  $j$ th object. Thus, for an intrinsically circular source with  $e^{(s)} = 0$ , we have

$$(52) \quad e = \frac{2g}{1 + |g|^2}.$$

In the weak lensing limit ( $|\kappa|, |\gamma| \ll 1$ ), equation (50) reduces to  $e^{(s)} \approx e - 2g \approx e - 2\gamma$ . Assuming the random orientation of the background sources, we average observed ellipticities over a sufficient number of images to obtain

$$(53) \quad \langle e \rangle \approx 2g \approx 2\gamma.$$

For  $g^{(\text{true})} = 0.1$ , the weak lensing approximation (53) gives  $g^{(\text{est})} = 0.099$ , or a negative bias of  $-1\%$ . For  $g^{(\text{true})} = 0.4$  in the non-linear regime, equation (53) gives  $g^{(\text{est})} = 0.345$ , corresponding to a negative bias of  $-14\%$ .

For a practical application of weak lensing shape measurements, we must take into account various observational effects such as noise in the shape measurement due to readout and/or sky background and the dilution of the lensing signal due to the isotropic/anisotropic point-spread function (PSF) effects. Thus, one cannot simply use equation (53) to measure the gravitational shear field. KSB took into account explicitly the Gaussian weight function in calculations of noisy shape moments and the effect of quadrupole PSF anisotropy, as well as isotropic PSF smearing, and derived in the limit of linear anisotropies relevant transformation equations between unlensed (intrinsic) and lensed (observed) ellipticities. In the limit of linear anisotropies, the transformation equation between the intrinsic and the observed complex ellipticities is formally expressed as

$$(54) \quad e_\alpha = e_\alpha^{(s)} + (C^g)_{\alpha\beta} g_\beta + (C^q)_{\alpha\beta} q_\beta,$$

where  $q_\alpha$  is the spin-2 PSF anisotropy kernel, and  $C$ s are linear response coefficients for the spin-2 anisotropy fields ( $g_\alpha$  and  $q_\alpha$ ), which can be calculated from observable weighted shape moments of galaxies and stellar objects[4, 50, 51]. In practical observations, the spin-2 PSF anisotropy  $q(\boldsymbol{\theta})$  can be measured from image ellipticities of foreground stars, for which both of  $e^{(s)}$  and  $g$  vanish:  $q_\beta(\boldsymbol{\theta}) = (C^q)_{\alpha\beta}^{-1} e_\alpha^*$ . As an example, we show in Figure 7 the quadrupole PSF anisotropy field as measured from stellar ellipticities before and after the anisotropic PSF correction using the Subaru  $i'$  data of the cluster A1689[9]. Figure 8 shows the distribution of stellar ellipticity components before and after the PSF anisotropy correction, corresponding to Figure 7.

Assuming that the expectation value of the intrinsic source ellipticity vanishes, we have the linear relation between the averaged image ellipticity and the reduced shear as

$$(55) \quad g_\alpha \approx \langle (C^g)_{\alpha\beta}^{-1} (e - C^q q)_\beta \rangle.$$

In the context of the KSB formalism, the linear response  $C_{\alpha\beta}^g$  to the gravitational shear is often denoted as  $P_{\alpha\beta}^g$  (or  $P_{\alpha\beta}^\gamma$ ). A careful calibration of  $P^g$  is crucial for accurate measurements of the weak lensing signal. See Refs. [52] and [53] for more detailed discussions on the shear calibration issues.

**3.3.  $E/B$  Decomposition.** – In general, the shear tensor field  $\Gamma_{\alpha\beta}(\boldsymbol{\theta}) = \gamma_1(\boldsymbol{\theta})\sigma_3 + \gamma_2(\boldsymbol{\theta})\sigma_1$  that describes the spin-2 quadrupole shape distortions can be expressed as a sum of two terms, corresponding to two degrees of freedom, by introducing two scalar functions  $\Phi_E(\boldsymbol{\theta})$  and  $\Phi_B(\boldsymbol{\theta})$  (see Ref. [43]) as

$$(56) \quad \Gamma_{\alpha\beta}(\boldsymbol{\theta}) = \begin{pmatrix} \gamma_1 & \gamma_2 \\ \gamma_2 & -\gamma_1 \end{pmatrix} = \Gamma_{\alpha\beta}^{(E)}(\boldsymbol{\theta}) + \Gamma_{\alpha\beta}^{(B)}(\boldsymbol{\theta}),$$

$$(57) \quad \Gamma_{\alpha\beta}^{(E)} = \left( \partial_\alpha \partial_\beta - \delta_{\alpha\beta} \frac{1}{2} \Delta_\theta \right) \Phi_E(\boldsymbol{\theta}); \quad \Gamma_{\alpha\beta}^{(B)} = \frac{1}{2} (\epsilon_{\gamma\beta} \partial_\alpha \partial_\gamma + \epsilon_{\gamma\alpha} \partial_\beta \partial_\gamma) \Phi_B(\boldsymbol{\theta}),$$

where  $\epsilon_{\alpha\beta}$  is the  $2 \times 2$  antisymmetric tensor,  $\epsilon_{11} = \epsilon_{22} = 0$ ,  $\epsilon_{12} = -\epsilon_{21} = 1$ . The first term associated with  $\Phi_E$  is a gradient or scalar  $E$  component, and the second term with  $\Phi_B$  is a curl or pseudoscalar  $B$  component. The  $\gamma_1$  and  $\gamma_2$  are then written in terms of  $\Phi_E$  and  $\Phi_B$  as

$$(58) \quad \gamma_1 = +\Gamma_{11} = -\Gamma_{22} = \frac{1}{2} (\Phi_{E,11} - \Phi_{E,22}) - \Phi_{B,12}$$

$$(59) \quad \gamma_2 = \Gamma_{12} = \Gamma_{21} = \Phi_{E,12} + \frac{1}{2} (\Phi_{B,11} - \Phi_{B,22}).$$

As we have seen in §3.1, the spin-2  $\gamma$  field is coordinate dependent, which transforms as  $\gamma' = \gamma e^{2i\varphi}$  under a rotation of the basis axis by  $\varphi$ . The  $E$  and  $B$  parts can be extracted from the shear tensor by applying the  $\nabla_\theta^4$  operator:

$$(60) \quad 2\nabla_\theta^2 \kappa_E \equiv \nabla_\theta^4 \Phi_E = 2\partial^\alpha \partial^\beta \Gamma_{\alpha\beta}, \quad 2\nabla_\theta^2 \kappa_B \equiv \nabla_\theta^4 \Phi_B = 2\epsilon_{\alpha\beta} \partial^\alpha \partial^\gamma \Gamma_{\beta\gamma},$$

where we have defined the  $E$  and  $B$  fields,  $\kappa_E = (1/2)\Delta_\theta \Phi_E$  and  $\kappa_B = (1/2)\Delta_\theta \Phi_B$ , respectively. This technique is called as the  $E$ - $B$  mode decomposition. The above equations tell us that the relations between the  $E/B$ -fields and the spin-2 field are intrinsically non-local.

Remembering that in the case of gravitational lensing the shear tensor is given as  $\Gamma_{\alpha\beta} = (\partial_\alpha \partial_\beta - \delta_{\alpha\beta} \Delta_\theta / 2) \psi(\boldsymbol{\theta})$ , we can identify  $\Phi_E(\boldsymbol{\theta}) = \psi(\boldsymbol{\theta})$  and  $\Phi_B(\boldsymbol{\theta}) = 0$ . Hence, for a lensing-induced shear field, the  $E$ -mode signal is related with the convergence  $\kappa$ , i.e., the surface mass density of the lens, while the  $B$ -mode signal is identically zero. We note that gravitational lensing can give rise to  $B$ -modes, for example, when multiple deflections of light rays along the light path are involved. However, these  $B$  modes arise at higher orders and the  $B$ -mode contributions coming from multiple deflections are suppressed by a large factor compared to the  $E$ -mode contributions. In practical observations, intrinsic ellipticities of background galaxies also contribute to the gravitational shear estimate,  $\gamma^{\text{est}}$ . Assuming that intrinsic ellipticities have random orientations in projection space, such uncorrelated ellipticities will yield statistically identical contributions to the  $E$ - and  $B$  modes. Thus the  $B$ -mode signals serve as a useful null check for systematic effects (e.g., residual PSF anisotropies).

Now we turn to the issue of  $E/B$ -mode reconstructions from the spin-2 shear field. Rewriting equations (60) and (60) in terms of the complex shear  $\gamma$ , we find

$$(61) \quad \Delta_\theta \kappa_E = \Re \left( 2\hat{\mathcal{D}}_\theta^* \gamma \right),$$

$$(62) \quad \Delta_\theta \kappa_B = \Im \left( 2\hat{\mathcal{D}}_\theta^* \gamma \right) = -\Re \left( 2\hat{\mathcal{D}}_\theta^* i\gamma \right).$$

Defining  $\kappa \equiv \kappa_E + i\kappa_B$ , we see that equations (61) and (62) are identical to the mass inversion equation (39). Therefore, the  $B$ -mode convergence  $\kappa_B$  can be simply obtained as the imaginary part of equation (41), which is expected to vanish for a purely weak lensing signal. Furthermore, the second equality of equation (62) indicates that the transformation  $\gamma'(\boldsymbol{\theta}) = i\gamma(\boldsymbol{\theta})$  ( $\gamma'_1 = -\gamma_2, \gamma'_2 = \gamma_1$ ) is equivalent to an interchange operation of the  $E$  and  $B$  modes of the original maps:  $\kappa'_E(\boldsymbol{\theta}) = -\kappa_B(\boldsymbol{\theta})$ ,  $\kappa'_B(\boldsymbol{\theta}) = \kappa_E(\boldsymbol{\theta})$ . Since  $\gamma$  is a spin-2 field that transforms as  $\gamma' = \gamma e^{2i\varphi}$ , this operation is also equivalent to a rotation of each ellipticity by  $\pi/4$  with each position vector fixed.

**3.4. Magnification Bias.** – In the absence of gravitational lensing, the cumulative number counts  $n_0(> S_0)$  (per solid angle) of background galaxies above the limiting flux  $S_0$  can be locally approximated around  $S = S_0$  by a power-law form:

$$(63) \quad n_0(> S_0) \equiv \int_{S_0}^{\infty} dS \frac{d^2 N}{d\Omega dS} \propto S_0^{-\alpha}$$

with the running power index around  $S = S_0$

$$(64) \quad \alpha \equiv -\frac{d \log_{10} n_0(> S_0)}{d \log_{10} S_0} > 0.$$

Note the value of  $\alpha$  depends on the luminosity function  $dn/dL(L, z)$  of background sources (and hence the object type, such as late/early type galaxies and quasars) and the observing wavelength.

Gravitational lensing induces the following conflicting effects known as *magnification bias* (see Refs. [54] and [55]):

1 Area distortion:  $\delta\Omega^I = \mu(\boldsymbol{\theta})\delta\Omega^S$

2 Flux Magnification:  $S \rightarrow \mu(\boldsymbol{\theta})S$ .

The former effect reduces the effective observing area in the source plane, decreasing the number of background sources per solid angle; on the other hand, the latter effect amplifies the flux of background sources, increasing the number of sources above the limiting flux. The net number counts with gravitational lensing is given as

$$(65) \quad n(> S_0) \equiv \int_{S_0/\mu}^{\infty} dS \frac{d^2 N}{\mu d\Omega dS} = \mu^{\alpha-1} n_0(> S_0).$$

This implies that, (i) positive bias for  $\alpha > 1$  and (ii) negative bias for  $\alpha < 1$ .

In the weak lensing limit ( $|\kappa|, |\gamma_\alpha| \ll 1$ ),

$$(66) \quad n(> S_0) \approx (1 + 2\kappa)^{\alpha-1} n_0(> S_0) \approx \{1 + 2(\alpha - 1)\kappa\} n_0(> S_0).$$

The fractional change in the surface number density of background sources is thus given as

$$(67) \quad \delta_N = \frac{\delta n}{n_0} \approx -2(1 - \alpha)\kappa.$$

Hence the magnification-bias  $\delta_N(\boldsymbol{\theta})$  in the weak-lensing limit is a local measure of the surface-mass density field,  $\kappa(\boldsymbol{\theta})$ . A combination of the lens distortion and magnification can thus be used to break the mass-sheet degeneracy inherent in the shear-based mass determination[8, 9].

#### 4. – Cluster Weak Lensing Profiles

In this section we summarize basic, useful techniques for measuring cluster weak lensing profiles, which can be compared quantitatively with various cluster models, and can be used to constrain cluster mass and structure parameters.

**4.1. Weak Lensing Distortion.** – The spin-2 shape distortion of an object due to gravitational lensing is described by the complex reduced shear,  $g = g_1 + ig_2 = \gamma/(1 - \kappa)$ , which however is coordinate dependent. For a given reference point on the sky, one can instead form coordinate-independent quantities, the tangential distortion  $g_+$  and the  $45^\circ$  rotated component, from linear combinations of the distortion coefficients  $g_1$  and  $g_2$  as[56]

$$(68) \quad g_+ = -(g_1 \cos 2\varphi + g_2 \sin 2\varphi), \quad g_\times = -(g_2 \cos 2\varphi - g_1 \sin 2\varphi),$$

where  $\varphi$  is the position angle of an object with respect to the reference position, and the uncertainty in the  $g_+$  and  $g_\times$  measurement is  $\sigma_+ = \sigma_\times = \sigma_g/\sqrt{2} \equiv \sigma$  in terms of the rms error  $\sigma_g$  for the complex distortion measurement. The  $+$ -component,  $g_+$ , is a measure of tangential coherence of the shape distortions of background images due weak gravitational lensing (see Figure 5 and discussions in §3.3). On the other hand, the  $\times$ -component,  $g_\times$ , corresponds to divergence-free, curl-type distortion patterns of background images. In practice, the reference point is taken to be the cluster center, which can be determined from symmetry of the strong lensing pattern, the X-ray centroid position, or the brightest cluster galaxy position[13]. To improve the statistical significance of the distortion measurement, we calculate the weighted average of the  $g_+$ 's and its weighted error as

$$(69) \quad \langle g_+(\theta_n) \rangle = \frac{\sum_j u_{g,j} g_{+,j}}{\sum_j u_j}, \quad \langle g_\times(\theta_n) \rangle = \frac{\sum_j u_{g,j} g_{\times,j}}{\sum_j u_j},$$

$$(70) \quad C_{mn} \equiv \langle \Delta g_+(\theta_m) \Delta g_+(\theta_n) \rangle = \langle \Delta g_\times(\theta_m) \Delta g_\times(\theta_n) \rangle = \delta_{mn} \sigma_+^2(\theta_m)$$

$$(71) \quad \sigma_+(\theta_n) = \sigma_\times(\theta_n) = \left( \frac{\sum_j u_{g,j}^2 \sigma_j^2}{\left( \sum_j u_{g,j} \right)^2} \right)^{1/2},$$

$$(72) \quad \theta_n = \sum_{j \in \text{bin } n} u_{g,j} |\boldsymbol{\theta}_j| / \sum_{j \in \text{bin } n} u_{g,j},$$

where the  $j$  runs over all of the objects located within the  $n$ th annulus with a median radius of  $\theta_n$ ,  $g_{+,j}$  is the  $+$ -component of the reduced shear estimate for the  $j$ th object,

$u_{g,j}$  is a statistical weight for the  $j$ th object, and  $C_{mn}$  is the bin-to-bin covariance error matrix of the binned distortion profiles. Here we have used  $\langle g_{\alpha,i} g_{\beta,j} \rangle = (1/2) \sigma_{g,j}^2 \delta_{\alpha\beta} \delta_{ij}$  ( $\alpha, \beta = 1, 2$ ).<sup>(3)</sup> Several authors adopted the statistical weight  $u_{g,i}$  of the form:  $u_{g,i} = 1/(\sigma_{g,j}^2 + \alpha^2)$ , with  $\alpha$  being the softening constant variance [57, 58, 40]. In the limit of  $\alpha \gg \sigma_g^2$ , this corresponds to the uniform weighting. The case of  $\alpha = 0$  is known as the inverse-variance weighting, yielding  $\sigma_+(\theta_n) = \sigma_-(\theta_n) = 1/\sqrt{\sum_j (1/\sigma_j^2)}$ . In Refs. [57] and [7]  $\alpha \sim \langle \sigma_g^2 \rangle \approx 0.4$  was used as the softening parameter for the weight function.

The tangential reduced shear  $g_+(\theta)$  as a function of angular radius is a useful, direct observable in weak lensing observations, being free from the mass-sheet degeneracy (§3.1): It does not require a non-local mass reconstruction (see §3.1 and 3.3), and hence one can easily assess its error propagation as given by equations (70) and (71). In particular, the bin-to-bin covariance error matrix  $C_{mn}$  is diagonal (assuming that statistical uncertainties are dominated by random orientations of intrinsic ellipticities). Furthermore, the 45°-rotated  $g_\times$  component can be used as a useful null check for systematic effects. To compare observed tangential-distortion profiles with cluster mass models, one can use the identity  $\langle \gamma_+(\theta) \rangle = \bar{\kappa}(<\theta) - \langle \kappa(\theta) \rangle$  [4][5], where  $\langle \gamma_+(\theta) \rangle$  is the azimuthally-averaged tangential component of the gravitational shear at radius  $\theta$ ,  $\langle \kappa(\theta) \rangle = \langle \Sigma_m(\theta) \rangle / \Sigma_{\text{crit}}$  is the azimuthally-averaged  $\kappa$  at radius  $\theta$ , and  $\bar{\kappa}(<\theta) = \bar{\Sigma}_m(<\theta) / \Sigma_{\text{crit}}$  is the mean lensing convergence interior to radius  $\theta$ . If the projected cluster mass distribution is azimuthally symmetric about its center, then one can make an approximation  $\langle g_+(\theta) \rangle \simeq (\bar{\kappa}(<\theta) - \langle \kappa(\theta) \rangle) / (1 - \langle \kappa(\theta) \rangle)$  to compare with predictions from azimuthally-symmetric mass models (see Table 1).

In Figure 9 we show the tangential and 45°-rotated distortion profiles for A1689 at  $z_d = 0.183$  (*left*) and A2142 at  $z_d = 0.091$  (*right*) derived from Subaru weak lensing data [59, 9, 60], along with the respective best-fitting  $g_+(\theta)$ -profiles for the NFW (see Ref. [37]) and singular isothermal sphere (SIS) models (see Table 1). In both cases, the cluster distortion profiles are better fitted by the NFW model with a continuously steepening profile. For the nearby, high-mass cluster A2142, the curvature in the distortion profile appears highly pronounced, and the SIS model can be strongly rejected by the weak lensing data alone.

**4.2. Weak Lensing Depletion.** – Lensing magnification  $\mu$  influences the observed surface density of background sources, expanding the area of sky, and enhancing the observed flux of background sources (§3.4). For red background galaxies at a median redshift of  $\bar{z}_s \sim 1$ , the intrinsic count slope  $s = -d \log_{10} n_0(> S_0) / d \log_{10} S_0 = (5/2) d \log_{10} n(< m_0) / dm_0$  at faint magnitudes  $m_0$  is relatively flat ( $s < 1$ ), so that a net count depletion results [54]. Recently the count depletion of red background galaxies due to gravitational lensing has been clearly detected in several massive clusters (A1689, A1703, A370, RXJ1347-11, CL0024+1654) [8, 12, 40]. Figure 10 displays the count-depletion profile derived from a Subaru  $BR_c z'$ -selected red galaxy sample in the background of CL0024+1654 at  $z_s = 0.395$  [40]. The error bars include not only the Poisson contribution but also the variance due to variations of the counts along the azimuthal direction, i.e., contributions from the intrinsic clustering of red galaxies [54, 61] and departure from

---

<sup>(3)</sup> We have ignored the contribution of large scale structure along the line of sight to the lensing signal, namely the cosmic shear signal, acting as spatially correlated noise on the cluster lensing measurement. See Ref. [35].

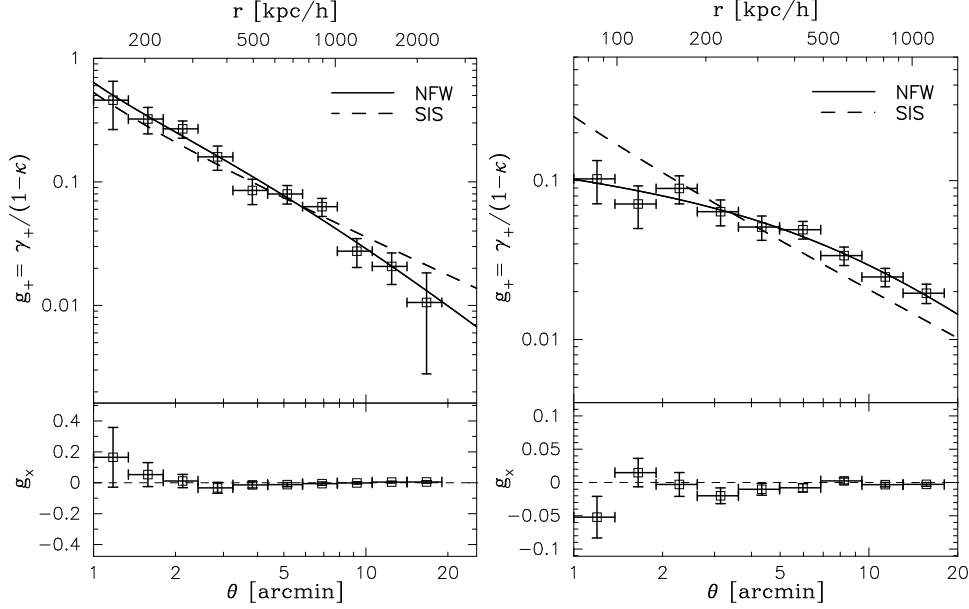


Fig. 9. – Azimuthally-averaged radial profiles of the tangential reduced shear  $g_+$  (*upper panels*) for the high-mass galaxy clusters A1689 at  $z_d = 0.183$  (*left*) and A2142 at  $z_d = 0.091$  (*right*) based on deep Subaru weak lensing data. The solid and dashed curves show the best-fitting NFW and SIS profiles for each cluster. Shown below is the  $45^\circ$  rotated ( $\times$ ) component,  $g_\times$ . Figure taken from Ref. [60].

circular symmetry[9]. A strong depletion of the red galaxy counts is shown in the central, high-density region of the cluster, and clearly detected out to a few arcminutes from the cluster center. The gray-filled region represents the 68.3% confidence bounds for the predicted count depletion curve  $n(\theta) = n_0 \mu^{s-1}(\theta)$  from an NFW model constrained by Subaru distortoin data, demonstrating clear consistency between these two independent lensing observables.

**4.3. Weak Lensing Dilution.** – It is crucial in the cluster weak lensing analysis to make a secure selection of background galaxies in order to minimize contamination by cluster/foreground galaxies and hence to make an accurate determination of the cluster mass, otherwise dilution of the distortion signal results from the inclusion of unlensed cluster galaxies, particularly at small radius where the cluster is relatively dense[59][42].

This dilution effect is simply to reduce the strength of the lensing signal when averaged over a local ensemble of galaxies, in proportion to the fraction of unlensed cluster and foreground galaxies whose orientations are randomly distributed, thus diluting the lensing signal relative to the true background level, derived from the uncontaminated background population[42]. With a pure red background sample (B) as a reference, one can quantify the *degree of dilution* for a galaxy sample (G) containing  $N_{\text{CL}}$  cluster galaxies and  $N_{\text{BG}}$  background galaxies in terms of the strengths of the averaged tangential shear signal

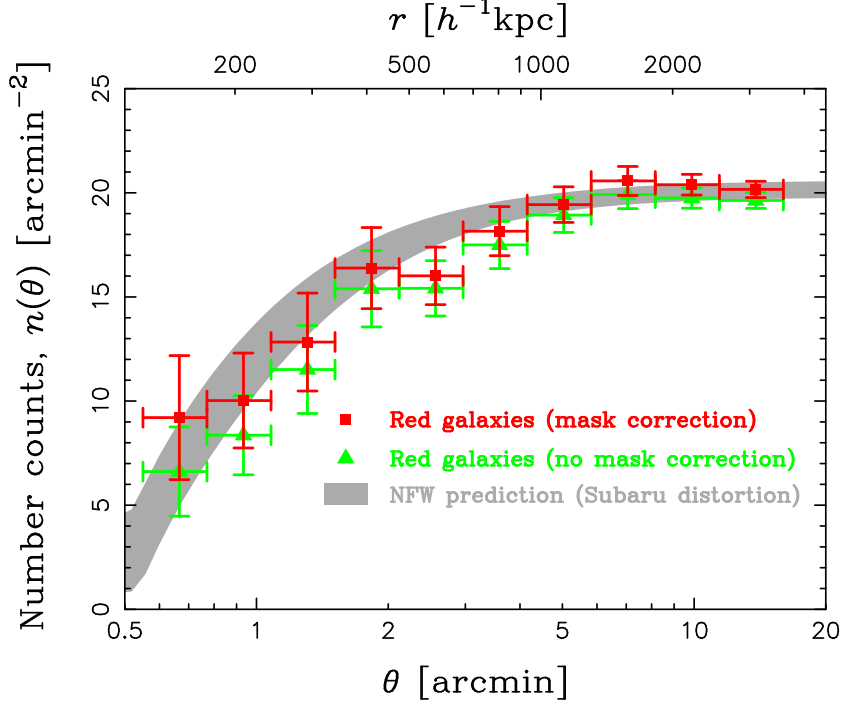


Fig. 10. – Number-count profile of Subaru  $BR_{cz}'$ -selected red galaxies (*squares*) in the background of Cl0024+1654 at  $z_d = 0.395$ . The triangles show the counts without the mask correction due to cluster members and bright foreground objects. A slight dip at  $\theta = 2' - 3'$  in the depletion profile corresponds to the contribution of the known substructure (see Figure 6), which is also seen in Subaru distortion data. The gray-filled region represents the 68.3% confidence bounds for the predicted count depletion curve from an NFW model constrained by our Subaru distortion analysis, demonstrating clear consistency between these two independent lensing observables. Figure taken from Ref. [40].

$\langle g_+(\theta) \rangle$  as[42]

$$(73) \quad 1 + \delta_d(\theta) \equiv \frac{N_{BG} + N_{CL}}{N_{BG}} = \frac{\langle g_+^{(B)}(\theta) \rangle \langle D_{ds}/D_s \rangle_{z_s \neq z_d}^{(G)}}{\langle g_+^{(G)}(\theta) \rangle \langle D_{ds}/D_s \rangle_{z_s \neq z_d}^{(B)}},$$

where  $\langle D_{ds}/D_s \rangle_{z_s \neq z_d}$ 's are averaged distance ratios for respective background populations<sup>(4)</sup>; if the two samples contain the same background population, then  $\delta_d = \langle g_+^{(B)} \rangle / \langle g_+^{(G)} \rangle - 1$ . The degree of dilution thus varies depending on the radius from the cluster center, increasing towards the cluster center. Medezinski et al. [42] found for their *green* galaxy sample ( $[V - i']_{E/S0-0.3}^{+0.1}$ ) containing the cluster sequence galaxies in A1689 that the fraction of cluster membership,  $N_{CL}/(N_{BG} + N_{CL})$ , tends  $\sim 100\%$  within

<sup>(4)</sup> *Background* samples can be generalized to include foreground field galaxies with  $z_s < z_d$  and  $D_{ds}/D_s(z_s) = 0$

$R \lesssim 300 \text{ kpc } h^{-1}$ .

Broadhurst, Takada, Umetsu et al. (see Ref. [59]) proposed to use a sample of *red background galaxies* whose colors are redder due to large  $k$ -corrections than the color-magnitude relation, or red sequence, of cluster member galaxies. These red background galaxies are largely composed of early to mid-type galaxies at moderate redshifts[42]. Cluster member galaxies are not expected to extend to these colors in any significant numbers because the intrinsically reddest class of cluster galaxies, i.e. E/S0 galaxies, are defined by the red sequence and lie blueward of chosen sample limit, so that even large photometric errors will not carry them into such a red sample. This can be demonstrated readily, as shown in Figure 11, where we plot the mean tangential shear strength  $\langle g_+ \rangle$  of A1689, averaged over a wide radial range of  $1' < \theta < 18'$ , as a function of color limit by changing the lower color limit progressively blueward. Here we do not apply area weighting to enhance the effect of dilution in the central region. Figure 11 shows a sharp drop in the lensing signal at  $\Delta(V - i') \lesssim 0.1$ , when the cluster red sequence starts to contribute significantly, thereby reducing the mean lensing signal. At  $\Delta(V - i') \gtrsim 0.1$ , the mean lensing signal of the red background stays fairly constant,  $\langle g_+ \rangle \simeq 0.143$ , ensuring that our weak lensing measurements are not sensitive to this particular choice of the color limit.

Recently, this empirical background selection method has been generalized by Medezinski, Broadhurst, Umetsu et al. [62] to incorporate and combine all color and positional information in a color-color (CC) diagram. This CC-selection method has been successfully applied to Subaru imaging observations of several massive clusters[62, 40].

On the other hand, the dilution of the lensing signal caused by cluster members can be used to derive the proportion of galaxies statistically belonging to the cluster, or the cluster member fraction, by comparing the undiluted background distortion signal with the radial distortion profile of color-magnitude (or color-color) space occupied by the cluster members, but including inevitable background galaxies falling in the same space[42]. This technique allows the light profile of the cluster to be determined in a way which is independent of the number density fluctuations in the background population, which otherwise limit the calculation of the cluster light profiles and luminosity functions from counts of member galaxies. The resulting light profile can be compared with the mass profile to examine the radial behavior of  $M/L$ [42, 62].

**4.4. Aperture Mass Densitometry.** – The observed image distortion of background galaxies can be directly used to derive the projected gravitational mass of clusters. The aperture mass estimate within the angular radius  $\theta$ ,  $M_\zeta(< \theta)$ , in terms of the tangential component  $\gamma_+$  of the gravitational shear can be expressed as

$$(74) \quad M_\zeta(< \theta) = \pi(D_d \theta)^2 \Sigma_{\text{crit}} \zeta(\theta),$$

using the aperture-mass densitometry, or the so-called “ $\zeta$ -statistic” [65], defined as

$$(75) \quad \zeta(\theta) \equiv \frac{2}{1 - \theta^2/\theta_{\text{out}}^2} \int_{\theta}^{\theta_{\text{out}}} d \ln \theta \langle \gamma_+(\theta) \rangle = \bar{\kappa}(< \theta) - \bar{\kappa}(\theta, \theta_{\text{out}}),$$

where  $\theta_{\text{out}}(> \theta)$  is the (constant) outer background radius,  $\langle \gamma_+(\theta) \rangle = \bar{\kappa}(< \theta) - \langle \kappa(\theta) \rangle$  is an azimuthal average of the tangential component of the gravitational shear at radius  $\theta$ , and  $\bar{\kappa} \equiv \bar{\Sigma}_m / \Sigma_{\text{crit}}$  is the mean convergence. Errors on  $\zeta(\theta)$  are calculated by propagating the rms errors  $\sigma_+(\theta_n)$  (equation [71]) for the tangential shear measurement. Equations



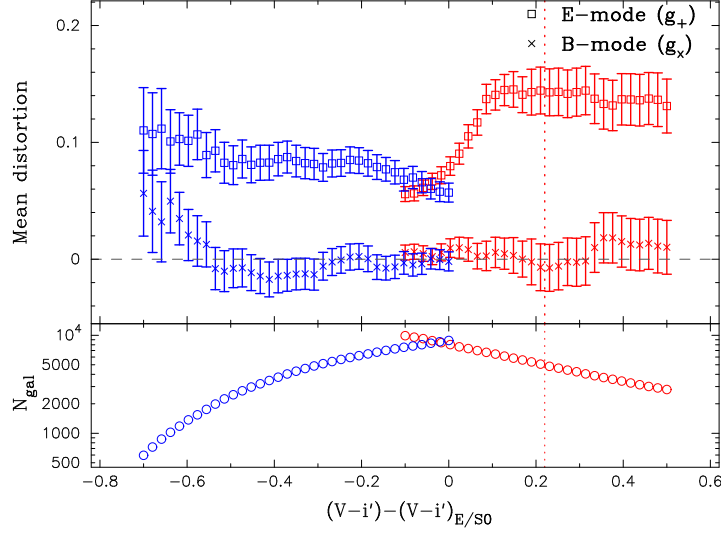


Fig. 11. – Top panel: mean distortion strength averaged over a wide radial range of  $1' < \theta < 18'$  of A1689, done separately for the blue and red galaxy samples. No area weighting is used here to enhance the effect of dilution in the central cluster region. Shown are the measurements of the tangential component ( $g_+$ ) with open squares, and those of the 45deg-rotated component ( $g_x$ ). Bottom panel: the respective numbers of galaxies as a function of color limit, contained in the range  $1' < \theta < 18'$  in the red (*right*) and the blue (*left*) samples. This figure is taken from Ref. [9].

(74) and (75) show that the cluster mass can be measured from the galaxies ellipticity within the annulus bounded by  $\theta$  and  $\theta_{\text{out}}$  located just *outside* the mass to be measured. In the weak lensing regime where  $|\kappa|, |\gamma| \ll 1$ ,  $\langle \gamma_+(\theta) \rangle$  is observable:  $\langle g_+(\theta) \rangle \approx \langle \gamma_+(\theta) \rangle$ .

As revealed in equation. (75), the  $\zeta$ -statistic yields a mean convergence interior to  $\theta$ , subtracted by the mean background within the annulus between  $\theta$  and  $\theta_{\text{out}}$ ,  $\bar{\kappa}(<\theta) - \bar{\kappa}(\theta, \theta_{\text{out}})$ . Hence, as long as  $\bar{\kappa}(\theta, \theta_{\text{out}}) \ll \bar{\kappa}(<\theta)$ , the enclosed mass within  $\theta$  can be obtained by multiplying  $\zeta$  by the area  $\pi \Sigma_{\text{crit}} (D_d \theta)^2$ . The inner radius  $\theta$  can almost be arbitrarily chosen to obtain the aperture mass interior to  $\theta$ , as long as the weak lensing approximation is valid. Obviously, the aperture mass is smaller than the enclosed mass by a negative compensating mass that serves to remove the contribution from a background uniform mass sheet, and the degree of deviation depends on how steep the density profile is.

The  $\zeta$ -statistic is a circular aperture mass estimator. It gives rise to some errors for irregular and merging clusters. Nevertheless, this effect has been estimated less than 10% [63]. The choice of the parameter  $\theta_{\text{out}}$  may also affect the cluster mass estimate in a practical application. For example, a small  $\theta_{\text{out}}$  will generate large Poisson noise since the galaxy number for a shear estimate within the annulus bound by  $\theta$  and  $\theta_{\text{out}}$  is not sufficiently large. On the other hand, if  $\theta_{\text{out}}$  is too large, the cluster mass measurement can be contaminated by neighboring clusters in projection. For a projected lens system,  $\langle \gamma_+ \rangle$  is produced not only by the cluster itself but also by the projected neighboring clusters and large scale structure.

Clowe et al. [64] proposed a variant of aperture mass densitometry [65], by introducing

two parameters to specify the annular background region, of the form:

$$(76) \quad \begin{aligned} \zeta_c(\theta) &\equiv 2 \int_{\theta}^{\theta_{\text{inn}}} d \ln \theta' \langle \gamma_+(\theta') \rangle + \frac{2}{1 - (\theta_{\text{inn}}/\theta_{\text{out}})^2} \int_{\theta_{\text{inn}}}^{\theta_{\text{out}}} d \ln \theta' \langle \gamma_+(\theta') \rangle \\ &= \bar{\kappa}(< \theta) - \bar{\kappa}(\theta_{\text{inn}}, \theta_{\text{out}}), \end{aligned}$$

where  $\theta_{\text{inn}}$  and  $\theta_{\text{out}}$  ( $\theta_{\text{out}} > \theta_{\text{inn}} > \theta$ ) are the inner and outer radii of the annular background region in which the mean background contribution,  $\bar{\kappa}_b \equiv \bar{\kappa}(\theta_{\text{inn}}, \theta_{\text{out}})$ , is defined. This cumulative mass estimator is often referred to as the  $\zeta_c$ -statistic. This cumulative mass estimator subtracts from the mean convergence  $\bar{\kappa}(\theta)$  a constant  $\bar{\kappa}_b$  for all apertures  $\theta$  in the measurements, thus removing any DC component in the control region  $\theta = [\theta_{\text{inn}}, \theta_{\text{out}}]$ . We note that the  $\bar{\kappa}_b$  is a non-observable free parameter. The  $\zeta_c$ -statistic will be particularly useful for wide-field imaging observations, such as with the Suprime-Cam on the Subaru telescope ( $34' \times 27'$ ) and the Megacam on the CFHT ( $1^\circ \times 1^\circ$ ), in which one can identify a background region well outside of the cluster region.

**4.5. Weak Lensing Convergence.** – Umetsu & Broadhurst [9] have developed a non-parametric method for reconstructing the one-dimensional  $\kappa$ -profile utilizing the  $\zeta_c$ -statistic measurement. Unlike strong-lensing based boundary conditions[8], this method utilizes an outer boundary condition on the mean background density  $\bar{\kappa}_b$  to derive a  $\kappa$ -profile (see Schneider & Seitz 1995 for an alternative method for a direct inversion of the mass profile).<sup>(5)</sup> For a given boundary condition  $\bar{\kappa}_b$ , the average convergence  $\bar{\kappa}(< \theta)$  is estimated as  $\bar{\kappa}(< \theta) = \zeta_c(\theta) + \bar{\kappa}_b$ . Then, we define a discretized estimator for  $\kappa$  as

$$(77) \quad \kappa(\bar{\theta}_m) = \alpha_2^m \zeta(\theta_{m+1}) - \alpha_1^m \zeta(\theta_m) + \bar{\kappa}_b,$$

where

$$(78) \quad \alpha_1^m = \frac{1}{2\Delta \ln \theta_m} \left( \frac{\theta_m}{\bar{\theta}_m} \right)^2, \quad \alpha_2^m = \frac{1}{2\Delta \ln \theta_m} \left( \frac{\theta_{m+1}}{\bar{\theta}_m} \right)^2,$$

and  $\bar{\theta}_m$  is the weighted center of the  $m$ th radial bin bounded by  $(\theta_m, \theta_{m+1})$  (see Refs. [9] and [40]). The error covariance matrix  $C_{mn}$  of  $\kappa_m$  is expressed as

$$C_{mn} = \alpha_2^m \alpha_2^n C_{m+1, n+1}^\zeta + \alpha_1^m \alpha_1^n C_{m, n}^\zeta - \alpha_1^m \alpha_2^n C_{m, n+1}^\zeta - \alpha_2^m \alpha_1^n C_{m+1, n}^\zeta,$$

where  $C_{mn}^\zeta \equiv \langle \delta \zeta_m \delta \zeta_n \rangle$  is the bin-to-bin error covariance matrix of the aperture densitometry measurements which is calculated by propagating the rms errors  $\sigma_+(\theta_m)$  for the tangential shear measurement (see §4.1). In the non-linear regime, however, the  $\gamma_+(\theta)$  is not a direct observable. Therefore, non-linear corrections need to be taken into account in the mass reconstruction process. In the subcritical regime (i.e., outside the critical curves), the  $\gamma_+(\theta)$  can be expressed in terms of the averaged tangential reduced shear as  $\langle g_+(\theta) \rangle \approx \gamma_+(\theta)/[1 - \kappa(\theta)]$  assuming a quasi circular symmetry in the projected mass distribution. This non-linear equation (76) for  $\zeta_c(\theta)$  can be solved by an iterative procedure, which is outlined in Ref. [40].

---

<sup>(5)</sup> The mass-sheet degeneracy is inevitable in any mass reconstruction method based solely on the shearing effect.

In the left panel of Figure 12 we show cluster surface mass density profiles  $\Sigma_m(\theta)$  for A1689[9] and CL0024+1654[40] as reconstructed from combined Subaru weak-lensing ( $r \gtrsim 200$  kpc) and HST/ACS strong-lensing ( $r \lesssim 200$  kpc) observations. The joint mass profiles for the clusters continuously steepen out to their virial radii, and are well fitted with single NFW profiles, which provide a good description of the equilibrium density profiles of collisionless DM halos in cosmological  $N$ -body simulations. The right panel of Figure 12 shows two-dimensional marginalized constraints on the NFW model parameters ( $c_{\text{vir}}, M_{\text{vir}}$ ) derived for CL0024+1654 from the joint mass profile shown in the left panel. This figure demonstrates that combining strong and weak-lensing information (*grey contours*) significantly reduces the uncertainties on the profile parameters. Such non-parametric mass profiles are also useful when comparing the total matter distribution with cluster properties obtained from other wavelengths and/or approaches[66, 67, 68, 69].

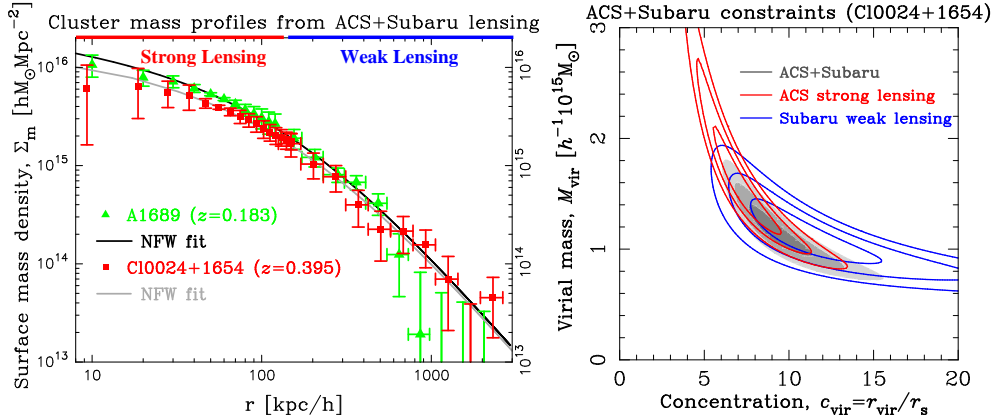


Fig. 12. – *Left*: Cluster surface mass density profiles for A1689 (*green triangles*) and CL0024+1654 (*red squares*) reconstructed from strong lensing (HST/ACS:  $r \lesssim 200$  kpc) and weak lensing measurements (Subaru:  $r \gtrsim 200$  kpc). The curvature of these profiles demonstrates that both strong and weak lensing data are required to make an accurate measurement of the cluster mass structure parameters, such as the halo virial mass,  $M_{\text{vir}}$ , and concentration,  $c_{\text{vir}}$ . Also shown as solid curves are the best-fit NFW models, with a continuously steepening density profile, for A1689 (*black*) and CL0024+1654 (*gray*). *Right*: Joint constraints on the NFW model parameters ( $c_{\text{vir}}, M_{\text{vir}}$ ) derived for CL0024+1654. The red and blue contours show the 68.3%, 95.4%, and 99.7% confidence limits for the inner strong lensing and outer weak lensing data, respectively. Combining strong and weak-lensing information (*gray contours*) significantly reduces the uncertainties on the profile parameters. Figures taken and modified from Umetsu & Broadhurst [9] and Umetsu, Medezinski, Broadhurst et al. [40].

## APPENDIX A.

### Multiple Lens Equation

We may discretize the cosmological lens equation (19) by dividing the radial integral between the source ( $\chi = \chi_s$ ) and the observer ( $\chi = 0$ ) into  $N$ -comoving boxes ( $N - 1$

lens-planes) separated by a comoving distance of  $\Delta\chi$ . The angular position  $\boldsymbol{\theta}^{(n)}$  of a light ray at the  $n$ th plane ( $n \leq N$ ) is then given by

$$(A.1) \quad \boldsymbol{\theta}^{(n)} - \boldsymbol{\theta}^{(0)} = - \sum_{p=1}^{n-1} \frac{r(\chi_n - \chi_p)}{r(\chi_n)} \nabla_{\perp} \psi_p$$

where  $\psi_p$  is the effective lensing potential of the  $p$ th lens plane ( $p = 1, 2, \dots, N-1$ ):

$$(A.2) \quad \psi_p = \frac{2}{c^2} \int_{\chi_p}^{\chi_p + \Delta\chi} d\chi \Psi.$$

The Jacobian matrix is expressed as

$$(A.3) \quad \mathbf{A}^{(n)} := \frac{\partial \boldsymbol{\theta}^{(n)}}{\partial \boldsymbol{\theta}^{(0)}} = \mathbf{I} - \sum_{p=1}^{n-1} g(\chi_p, \chi_n) \mathbf{H}^{(p)} \mathbf{A}^{(p)} \equiv \mathbf{I} - \boldsymbol{\Psi}^{(n)}$$

where  $H_{\alpha\beta}^{(p)} = \partial^2 \psi_p / \partial \chi^{\perp, \alpha} \partial \chi^{\perp, \beta}$  ( $\alpha, \beta = 1, 2$ ) is the Hessian matrix, and  $g(\chi_p, \chi_n)$  is the effective lensing distance for the  $p$ th lens plane. In general (without the Born approximation), the  $2 \times 2$  Jacobian matrix can be decomposed into the following form:

$$(A.4) \quad \mathcal{A}_{\alpha\beta} = \delta_{\alpha\beta} - \psi_{\alpha\beta} = (1 - \kappa) \delta_{\alpha\beta} - \gamma_1 \sigma_3 - \gamma_2 \sigma_1 - i\omega \sigma_2$$

where  $\kappa = (\psi_{11} + \psi_{22})/2$ ,  $\gamma_1 = (\psi_{11} - \psi_{22})/2$ ,  $\gamma_2 = (\psi_{12} + \psi_{21})/2$ , and  $\omega$  is the net rotation  $\omega = (\psi_{12} - \psi_{21})/2$ . The Born approximation  $\mathbf{A}^{(p)} = \mathbf{I}$  leads to the symmetric Jacobian matrix.

\* \* \*

I am very grateful to the organizers of the Fermi summer school, Y. Rephaeli and A. Cavaliere, for the invitation to present the research discussed in this review. I would like to thank Masahiro Takada and Patrick Koch for providing invaluable comments on the manuscript. This work is partially supported by the National Science Council of Taiwan under the grant NSC97-2112-M-001-020-MY3.

## REFERENCES

- [1] TYSON J. A., WENK R. A. and VALDES F., *ApJ*, **349** (1990) L1.
- [2] KAISER N. and SQUIRES G., *ApJ*, **404** (1993) 441.
- [3] SCHNEIDER P. and SEITZ C., *A&A*, **294** (1995) 411.
- [4] BARTELMANN M. and SCHNEIDER P., *Phys. Rep.*, **340** (2001) 291.
- [5] UMETSU K., TADA M. and FUTAMASE T., *Progress of Theoretical Physics Supplement*, **133** (1999) 53 (arXiv:astro-ph/0004400).
- [6] CLOWE D., BRADAČ M., GONZALEZ A. H., MARKEVITCH M., RANDALL S. W., JONES C. and ZARITSKY D., *ApJ*, **648** (2006) L109.
- [7] OKABE N. and UMETSU K., *PASJ*, **60** (2008) 345.
- [8] BROADHURST T., TAKADA M., UMETSU K., KONG X., ARIMOTO N., CHIBA M. and FUTAMASE T., *ApJ*, **619** (2005) L143.

- [9] UMETSU K. and BROADHURST T., *ApJ*, **684** (2008) 177 (arXiv:0712.3441).
- [10] LIMOUSIN M., RICHARD J., JULLO E., KNEIB J.-P., FORT B., SOUCAIL G., ELÍASDÓTTIR Á., NATARAJAN P., ELLIS R. S., SMAIL I., CZOSKE O., SMITH G. P., HUDELLOT P., BARDEAU S., EBELING H., EGAMI E. and KNUDSEN K. K., *ApJ*, **668** (2007) 643.
- [11] MANDELBAUM R., SELJAK U. and HIRATA C. M., *JCAP*, **8** (2008) 6 (arXiv:0805.2552).
- [12] BROADHURST T., UMETSU K., MEDEZINSKI E., OGURI M. and REPHAELI Y., *ApJ*, **685** (2008) L9.
- [13] OKABE N., TAKADA M., UMETSU K., FUTAMASE T. and SMITH G. P., *PASJ*, *submitted*, (2009) arXiv:0903.1103.
- [14] OGURI M., HENNAWI J. F., GLADDERS M. D., DAHLE H., NATARAJAN P., DALAL N., KOESTER B. P., SHARON K. and BAYLISS M., *ApJ*, **699** (2009) 1038.
- [15] JOHNSTON D. E., SHELDON E. S., WECHSLER R. H., ROZO E., KOESTER B. P., FRIEMAN J. A., MCKAY T. A., EVRARD A. E., BECKER M. R. and ANNIS J., (2007) arXiv:0709.1159
- [16] SPERGEL D. N., BEAN R., DORÉ O., NOLTA M. R., BENNETT C. L., DUNKLEY J., HINSHAW G., JAROSIK N., KOMATSU E., PAGE L., PEIRIS H. V., VERDE L., HALPERN M., HILL R. S., KOGUT A., LIMON M., MEYER S. S., ODEGARD N., TUCKER G. S., WEILAND J. L., WOLLACK E. and WRIGHT E. L., *ApJS*, **170** (2007) 377.
- [17] KOMATSU E., DUNKLEY J., NOLTA M. R., BENNETT C. L., GOLD B., HINSHAW G., JAROSIK N., LARSON D., LIMON M., PAGE L., SPERGEL D. N., HALPERN M., HILL R. S., KOGUT A., MEYER S. S., TUCKER G. S., WEILAND J. L., WOLLACK E. and WRIGHT E. L., *ApJS*, **180** (2009) 330.
- [18] SCHNEIDER P., *MNRAS*, **283** (1996) 837.
- [19] ERBEN T., VAN WAERBEKE L., MELLIER Y., SCHNEIDER P., CUILANDRE J.-C., CASTANDER F. J. and DANTEL-FORT M., *A&A*, **355** (2000) 23.
- [20] UMETSU K. and FUTAMASE T., *ApJ*, **539** (2000) L5 (arXiv:astro-ph/0004373).
- [21] MIYAZAKI S., HAMANA T., SHIMASAKU K., FURUSAWA H., DOI M., HAMABE M., IMI K., KIMURA M., KOMIYAMA Y., NAKATA F., OKADA N., OKAMURA S., OUCHI M., SEKIGUCHI M., YAGI M. and YASUDA N., *ApJ*, **580** (2002) L97.
- [22] MIYAZAKI S., HAMANA T., ELLIS R. S., KASHIKAWA N., MASSEY R. J., TAYLOR J. and REFREGIER A., *ApJ*, **669** (2007) 714.
- [23] HAMANA T., MIYAZAKI S., KASHIKAWA N., ELLIS R. S., MASSEY R. J., REFREGIER A. and TAYLOR J. E., *PASJ*, **61** (2009) 833.
- [24] SCHNEIDER P., EHLERS J. and FALCO E. E., *Gravitational Lenses (Berlin: Springer, Verlag)*, (1992) .
- [25] BLANDFORD R. D. and NARAYAN R., *Ann. Rev. Astron. Astrophys.*, **30** (1992) 311.
- [26] REFSDAL S. and SURDEJ J., *Rep. Prog. Phys.*, **57** (1994) 117.
- [27] NARAYAN R. and BARTELMANN M., *arXiv:astro-ph/9606001*, (1996) .
- [28] HATTORI M., KNEIB J. and MAKINO N., *Progress of Theoretical Physics Supplement*, **133** (1999) 1.
- [29] LEBACH D. E., COREY B. E., SHAPIRO I. I., RATNER M. I., WEBBER J. C., ROGERS A. E. E., DAVIS J. L. and HERRING T. A., *Physical Review Letters*, **75** (1995) 1439.
- [30] SCHNEIDER P., *A&A*, **143** (1985) 413.
- [31] SASAKI M., *Progress of Theoretical Physics*, **90** (1993) 753.
- [32] SEITZ S., SCHNEIDER P. and EHLERS J., *Classical and Quantum Gravity*, **11** (1994) 2345.
- [33] FUTAMASE T., *Progress of Theoretical Physics*, **93** (1995) 647.
- [34] TAKADA M., *Ph.D. thesis, Tohoku University, Japan*, (2000) .
- [35] HOEKSTRA H., *MNRAS*, **339** (2003) 1155.
- [36] KEETON C. R., *arXiv:astro-ph/0102341*, (2001) .
- [37] NAVARRO J. F., FRENK C. S. and WHITE S. D. M., *ApJ*, **490** (1997) 493.
- [38] BARTELMANN M., *A&A*, **313** (1996) 697.
- [39] WRIGHT C. O. and BRAINERD T. G., *ApJ*, **534** (2000) 34.
- [40] UMETSU K., MEDEZINSKI E., BROADHURST T., ZITRIN A., OKABE N., HSIEH B. and MOLNAR S. M., *ApJ*, *in press*, (2010) arXiv:0908.0069.
- [41] TAYLOR A. N., KITCHING T. D., BACON D. J. and HEAVENS A. F., *MNRAS*, **374** (2007) 1377.

- [42] MEDEZINSKI E., BROADHURST T., UMETSU K., COE D., BENÍTEZ N., FORD H., REPHAELI Y., ARIMOTO N. and KONG X., *ApJ*, **663** (2007) 717.
- [43] CRITTENDEN R. G., NATARAJAN P., PEN U.-L. and THEUNS T., *ApJ*, **568** (2002) 20.
- [44] BACON D. J., GOLDBERG D. M., ROWE B. T. P. and TAYLOR A. N., *MNRAS*, **365** (2006) 414.
- [45] OKURA Y., UMETSU K. and FUTAMASE T., *ApJ*, **660** (2007) 995 (arXiv:astro-ph/0607288).
- [46] OKURA Y., UMETSU K. and FUTAMASE T., *ApJ*, **680** (2008) 1 (arXiv:0710.2262).
- [47] KAISER N., *ApJ*, **439** (1995) L1.
- [48] JAIN B., SELJAK U. and WHITE S., *ApJ*, **530** (2000) 547.
- [49] MIYAZAKI S., KOMIYAMA Y., SEKIGUCHI M., OKAMURA S., DOI M., FURUSAWA H., HAMABE M., IMI K., KIMURA M., NAKATA F., OKADA N., OUCHI M., SHIMASAKU K., YAGI M. and YASUDA N., *PASJ*, **54** (2002) 833.
- [50] KAISER N., SQUIRES G. and BROADHURST T., *ApJ*, **449** (1995) 460.
- [51] ERBEN T., VAN WAERBEKE L., BERTIN E., MELLIER Y. and SCHNEIDER P., *A&A*, **366** (2001) 717.
- [52] HEYMANS C., VAN WAERBEKE L., BACON D., BERGE J., BERNSTEIN G., BERTIN E., BRIDLE S., BROWN M. L., CLOWE D., DAHLE H., ERBEN T., GRAY M., HETTERSCHIEDT M., HOEKSTRA H., HUDELLOT P., JARVIS M., KUIJKEN K., MARGONINER V., MASSEY R., MELLIER Y., NAKAJIMA R., REFREGIER A., RHODES J., SCHRABBACK T. and WITTMAN D., *MNRAS*, **368** (2006) 1323.
- [53] MASSEY R., HEYMANS C., BERGÉ J., BERNSTEIN G., BRIDLE S., CLOWE D., DAHLE H., ELLIS R., ERBEN T., HETTERSCHIEDT M., HIGH F. W., HIRATA C., HOEKSTRA H., HUDELLOT P., JARVIS M., JOHNSTON D., KUIJKEN K., MARGONINER V., MANDELBAUM R., MELLIER Y., NAKAJIMA R., PAULIN-HENRIKSSON S., PEEPLES M., ROAT C., REFREGIER A., RHODES J., SCHRABBACK T., SCHIRMER M., SELJAK U., SEMBOLONI E. and VAN WAERBEKE L., *MNRAS*, **376** (2007) 13.
- [54] BROADHURST T. J., TAYLOR A. N. and PEACOCK J. A., *ApJ*, **438** (1995) 49.
- [55] TAYLOR A. N., DYE S., BROADHURST T. J., BENITEZ N. and VAN KAMPEN E., *ApJ*, **501** (1998) 539.
- [56] TYSON J. A. and FISCHER P., *ApJ*, **446** (1995) L55+.
- [57] HAMANA T., MIYAZAKI S., SHIMASAKU K., FURUSAWA H., DOI M., HAMABE M., IMI K., KIMURA M., KOMIYAMA Y., NAKATA F., OKADA N., OKAMURA S., OUCHI M., SEKIGUCHI M., YAGI M. and YASUDA N., *ApJ*, **597** (2003) 98.
- [58] OKABE N. and UMETSU K., *PASJ*, **60** (2008) 345.
- [59] BROADHURST T., TAKADA M., UMETSU K., KONG X., ARIMOTO N., CHIBA M. and FUTAMASE T., *ApJ*, **619** (2005) L143.
- [60] UMETSU K., BIRKINSHAW M., LIU G.-C., WU J.-H. P., MEDEZINSKI E., BROADHURST T., LEMZE D., ZITRIN A., HO P. T. P., HUANG C.-W. L., KOCH P. M., LIAO Y.-W., LIN K.-Y., MOLNAR S. M., NISHIOKA H., WANG F.-C., ALTAMIRANO P., CHANG C.-H., CHANG S.-H., CHANG S.-W., CHEN M.-T., HAN C.-C., HUANG Y.-D., HWANG Y.-J., JIANG H., KESTEVEN M., KUBO D. Y., LI C.-T., MARTIN-COCHER P., OSHIRO P., RAFFIN P., WEI T. and WILSON W., *ApJ*, **694** (2009) 1643 (arXiv:0810.0969).
- [61] ZHANG P. and PEN U., *Physical Review Letters*, **95** (2005) 241302.
- [62] MEDEZINSKI E., BROADHURST T., UMETSU K., OGURI M., REPHAELI Y. and BENÍTEZ N., *ApJ*, *in press*, (2010) arXiv:0906.4791.
- [63] CLOWE D., DE LUCIA G. and KING L., *MNRAS*, **350** (2004) 1038.
- [64] CLOWE D., LUPPINO G. A., KAISER N. and GIOIA I. M., *ApJ*, **539** (2000) 540.
- [65] FAHLMAN G., KAISER N., SQUIRES G. and WOODS D., *ApJ*, **437** (1994) 56.
- [66] LEMZE D., BARKANA R., BROADHURST T. J. and REPHAELI Y., *MNRAS*, **386** (2008) 1092.
- [67] LEMZE D., BROADHURST T., REPHAELI Y., BARKANA R. and UMETSU K., *ApJ*, **701** (2009) 1336.
- [68] LAPÍ A. and CAVALIERE A., *ApJ*, **695** (2009) L125.
- [69] PENG E., ANDERSSON K., BAUTZ M. W. and GARMIRE G. P., *ApJ*, **701** (2009) 1283.